

Nonlinear stabilization of chiral modes in space-time modulated parametric oscillators

Scott Lambert,^{1,2,*} Elise Jaremko,² and Jayson Paulose^{1,2,†}

¹*Materials Science Institute and Institute for Fundamental Science, University of Oregon, Eugene, OR 97403*

²*Department of Physics, University of Oregon, Eugene, OR 97403*

Phase control of parametric modulation in coupled oscillator networks enables sculpting of dynamical states with desired spatiotemporal symmetries. Symmetry-aware Floquet analysis successfully predicts such states in linear systems, but whether their symmetry properties persist under nonlinearity remains largely unexplored. Here, we establish the existence of nonlinear chiral steady states in a trio of coupled parametric oscillators with modulation phases chosen to selectively amplify a circulating mode in the linearized system. We find that a cubic nonlinearity arrests exponential growth of the amplified mode, producing a steady finite-amplitude motion that retains the expected chirality. By exploiting space-time symmetry, we reduce the dynamics to a single averaged equation that quantitatively predicts nonlinear trajectories, steady-state amplitudes, and characteristic time scales. The chiral steady states possess finite basins of attraction and are accessible from wide ranges of initial conditions and system parameters. Finite-element simulations of elastic plate resonators quantitatively reproduce these features, establishing the relevance of the reduced model to realistic continuum systems. Our results demonstrate that desirable properties of linear time-modulated systems, such as chirality and directional amplification, persist into strongly nonlinear regimes, opening pathways to robust nonreciprocal signal routing and amplification in parametrically driven platforms.

I. INTRODUCTION

Parametric oscillators, which are driven by time-modulation of system parameters rather than direct forcing, represent a fundamental mechanism for mode-coupling and amplification with broad applications such as low-noise amplification in microwave [1, 2] and superconducting [3] circuits, quantum [4] and classical [5] squeezed state generation, and coherent frequency conversion [6]. Nonlinearities make new phenomena possible in these systems, such as the stabilization of parametrically amplified modes [7], hysteretic amplitude and phase jumps that can be used for sensitive measurement [8–10], and state switching between stabilized phase states [8]. An analogy between the two stabilized phase states in a nonlinear parametric oscillator (NPO) and the two states of an Ising spin suggests that coupled NPOs could find the ground state of random Ising models, an NP-hard problem [11–16]. The spontaneous breaking of symmetry between the two phase states across coupled NPOs can serve as a manifestation of a discrete time crystal [17–19].

The theory of isolated nonlinear parametric oscillators (NPOs) is now well-established [7], but the characterization of coupled systems of NPOs remains in development. While many studies have investigated the dynamics of coupled NPOs with identical in-phase parametric modulations occurring across all oscillators [14, 17, 20–23] which is relevant to Ising optimization and time crystallization, less is known about coupled NPOs where the time-modulation has identical periodicity across all oscillators (hence establishing a common time period for

the system) but has different phases on different oscillators. A phase offset in the parametric modulation of a pair of NPOs influences the modulation frequencies at which resonant steady states occur [15, 24], but the effect of phase variation on the resulting nonlinear trajectories was not analyzed. The *linear* analysis of rings of phase-shifted parametric oscillators has predicted chiral [25, 26] and one-way [27, 28] wave transport and amplification with potential applications in nonreciprocal response and switching [29]. Whether these properties can be stabilized in NPO circuits remains an open question.

Here, we show that phase offsets in parametric modulation enable robust chiral steady states in a minimal model of coupled NPOs. Specifically, we investigate the dynamics of a ring of three classical oscillators, which we term the *trimer*, with out-of-phase modulations designed to generate stable circulating states (Fig. 1). The phase offset of $2\pi/3$ between adjacent trimers renders the system chiral—that is, it breaks mirror symmetry—and endows it with space-time symmetry under a spatial displacement combined by a time shift. Each oscillator includes a stabilizing cubic nonlinearity that effectively stiffens the springs with greater displacement, and a linear damping term. Adjacent oscillators experience a non-modulated linear coupling.

Without nonlinearity, damping, and modulation, the motion of the system is completely described by its three normal modes, illustrated in Fig. 1: the fundamental mode with all masses in phase, and two degenerate traveling-wave modes where the masses peak and fall in a well-defined succession. A space-time symmetric modulation of the grounding springs at twice the traveling-wave mode frequency singles out one of the modes for amplification in the linear system, as explained by a symmetry-aware Floquet analysis [26]. We show that nonlinearity stabilizes the amplified mode while main-

* slamber5@uoregon.edu

† jppaulose@uoregon.edu

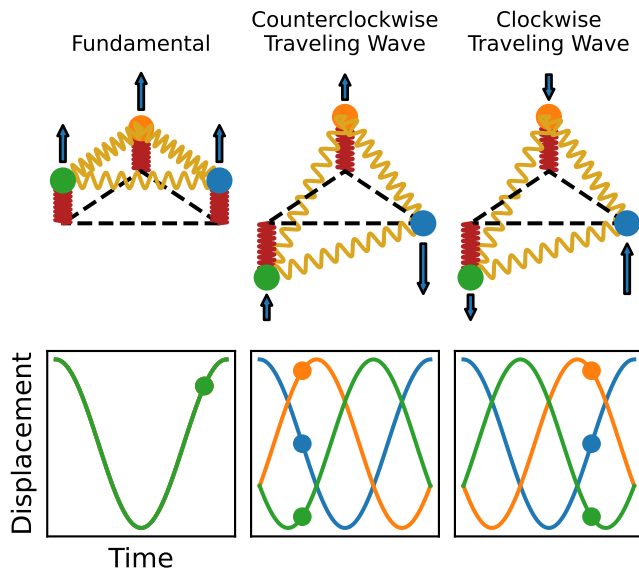


FIG. 1. The “trimer” model and its normal modes. Each colored disc represents an identical mass. Each grounding spring (red) has a time-modulated linear component and a nonlinear component. The modulation phase of each grounding spring increases by $2\pi/3$ moving one position clockwise around the trimer (blue \rightarrow green \rightarrow orange). The coupling springs (gold) add a linear restoring force in the vertical direction. The positions and blue arrows represent the displacements and velocities of the masses from snapshots of the three normal modes of the linear system without modulation. The dots indicate the times and positions of the motion that is shown in the diagrams.

taining its chirality: oscillations of the masses peak in a regular manner and in a definite order. We exploit the space-time symmetry to derive *reduced averaged equations* that describe the time-evolution of the amplified mode and reveal a variety of nonlinear coupled steady states, including persistent amplitude oscillations (for undamped motion) and convergence to a steady amplitude (with damping). A dynamical analysis of the reduced equations provides predictions for a variety of quantities of interest such as the steady-state amplitude and the time scales of its evolution, which we verify against numerical trajectories. We also numerically establish that the chiral steady states are attainable from a wide range of initial conditions: they reflect fixed points with finite, tunable basins of attraction in the phase space of the system.

While the idealized trimer system is amenable to exact analysis, we establish the relevance of our results to experiments by conducting finite-element simulations of coupled continuum plate resonators in which the requisite time-modulation and nonlinearity are recreated from the physics of elastic plates under tension [30, 31]. We show that the chiral nonlinear steady state is recreated in the continuum simulations, and that the reduced averaged equations—generated from three NPO degrees

of freedom—quantitatively describe features of the continuum trajectories with thousands of degrees of freedom. These results suggest that the chiral stabilized states are broadly generalizable to coupled NPO platforms that combine stabilizing nonlinearity and phase-controlled parametric modulation.

This paper will proceed as follows. In Section II, we introduce the trimer model and describe its behavior in the linear limit. In Section III, we derive the reduced averaged equations and use them to describe the trimer’s behavior, distinguishing between damped and undamped trimers. Finally, in Section IV, we show that some qualitative characteristics of the motions found in Section III carry over to a continuum system.

II. EQUATIONS OF MOTION AND LINEAR BEHAVIOR

The non-dimensionalized equations of motion for the trimer of coupled, anharmonic, damped, parametric oscillators described in Fig. 1 are

$$\ddot{x}_j + (1 + \delta \cos(\gamma t + \beta_j))x_j + \epsilon \dot{x}_j + x_j^3 + k(2x_j - x_{j+1} - x_{j-1}) = 0. \quad (1)$$

Here, $j \in \{1, 2, 3\}$ indexes the oscillators, and x_j is the displacement of oscillator j from equilibrium (with wraparound: $x_4 = x_1$ and $x_0 = x_3$). The dimensional equations and the non-dimensionalization procedure are presented in Appendix A. We have chosen the time unit so that the natural frequency of each oscillator (in isolation and without parametric modulation) is unity, and the length unit so that the cubic nonlinearity has unit coefficient. The parameters δ and γ respectively set the fractional strength and frequency of the parametric modulation, which acts only on the harmonic part of the individual oscillators. The phase offset β_j is set to

$$\beta_j = \frac{2\pi}{3}(j - 1) \quad (2)$$

to generate a traveling-wave modulation. Each oscillator experiences a linear damping with coefficient ϵ . The parameter δ quantifies the magnitude of the modulation, ϵ is the linear damping, and k is the coupling between adjacent oscillators. The linear eigenmodes of the system with $\delta = \epsilon = 0$ and ignoring the cubic term are shown in Fig. 1. The corresponding eigenfrequencies are $\omega = 1$ for the fundamental mode and $\omega = \sqrt{1 + 3k}$ for the degenerate traveling modes.

In the absence of nonlinearity, the time-modulated system can be analyzed using Floquet theory [26, 32]: the dynamics can be decomposed into a set of six *Floquet modes* $\vec{\psi}_i(t)$ that take the place of the normal modes. Each Floquet mode is a 6-vector of three displacements and three velocities; the six modes span the phase space of the trimer. The strobed dynamics of Floquet modes at integer multiples of the modulation period $T = 2\pi/\gamma$ is

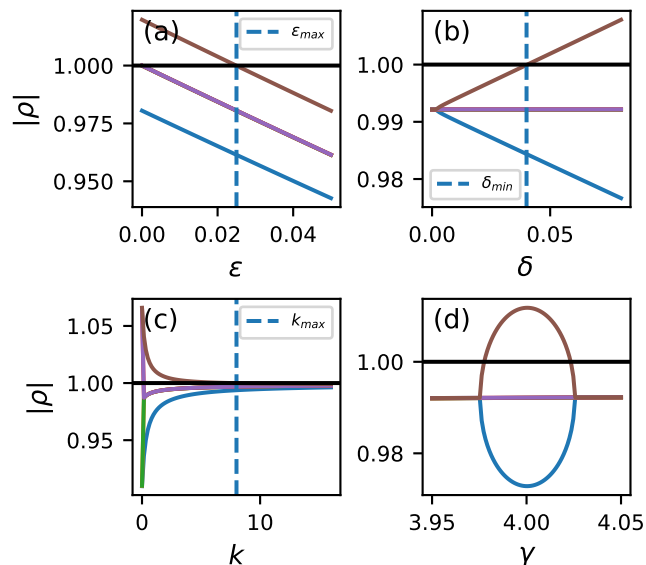


FIG. 2. Floquet spectra of the trimer at various parameter values. The colored lines are the absolute values of the Floquet eigenvalues of the system at the value of the parameter shown on the horizontal axis. When an eigenvalue exceeds $|\rho| = 1$ (black lines), amplification occurs. The vertical lines indicate values where the fixed point formula Eq. (32) predicts amplification will no longer occur. For the plots where ϵ , δ , and γ are varied, the other parameters are held fixed; the fixed values are $k = 1$, $\epsilon = 0.01$, $\delta = 0.1$, and $\gamma = 2\omega = 4$. For the plot with varied k , g is also varied to maintain the relationship $\gamma = 2\omega = 2\sqrt{1+3k}$.

simply $\vec{\psi}_i(t + 2\pi/\gamma) = \rho_i \vec{\psi}_i$, where ρ_i is the complex *Floquet multiplier* of the i th Floquet mode. Floquet modes with $|\rho_i| \neq 1$ signify exponentially growing or decaying modes. At finite damping, generically all Floquet modes decay over time ($|\rho_i| < 1$). However, at particular modulation parameters, some Floquet multipliers may have magnitude greater than one, signifying parametric resonances that feed energy into the system over many cycles.

The specific choice of modulation phases, Eq. (2), endows the system with a space-time symmetry: the equations of motion are unchanged upon simultaneously advancing time by $T/3$ and increasing the oscillator coordinate index by one. This symmetry constrains the parametric resonances of the system [26]. When the modulation frequency is set to twice the frequency of the traveling-wave normal modes, $\gamma = 2\omega$, only one mode is parametrically amplified, which smoothly connects to the counterclockwise normal mode as $\delta \rightarrow 0$. At zero damping, this mode is accompanied by an exponentially decaying Floquet mode which also rotates counterclockwise, but is offset by $\pi/2$ in its phase relative to the phase of the modulation. The other four Floquet modes, which derive from the fundamental mode and the clockwise traveling wave mode are not resonant, but are steady oscillations with $|\rho| = 1$ at zero damping. In Fig. 2(a), the Floquet multipliers of the parametrically amplified

and attenuated mode are shown in brown and blue respectively, while the other four modes are in purple and are seen to coincide at $|\rho| = 1$ when $\epsilon = 0$. As damping is turned on, the magnitudes of the Floquet multipliers are all reduced by damping, but the single amplified mode continues to be amplified until a threshold damping value (marked ϵ_{\max}) beyond which $|\rho|$ drops below one and all modes are attenuated.

The behavior of the parametric resonance on other system parameters is shown in the other panels of Fig. 2. As expected, the amplification rate of the amplified mode grows with the strength of the modulation (Fig. 2(b)). Increasing the coupling strength while keeping other parameters constant (but increasing the modulation frequency to maintain resonance conditions) leads to a reduction in the degree of amplification (Fig. 2(c)), since the modulation only acts on the grounding springs. Finally, the parametric resonance is predicted to occur exactly at $\gamma = 2\omega$ in the $\delta \rightarrow 0$ limit, but at finite modulation strengths, the resonance occurs for a range of modulation frequencies whose width about 2ω grows with δ (Fig. 2(d)). While all these resonance conditions can be derived using Floquet theory, we will recover them in our averaging analysis of the full nonlinear equations of motion in subsequent sections.

The linear theory of the trimer, and in particular its space-time symmetry, singles out the counterclockwise mode for parametric amplification, which occurs for finite ranges of the parameters and does not require fine tuning. Regardless of initial condition, we expect the linear dynamics to eventually be dominated by the resonant mode, which grows exponentially with time. Therefore, the system will eventually reach a regime where the nonlinear term becomes significant, regardless of the size of the initial displacements. In this work, we address the fate of the amplified mode due to the nonlinearity. We will find that the existence of the parametrically attenuated partner mode is crucial for the existence of convergent solutions at long times: the nonlinearity shifts the oscillation phases in tandem so that the parametric drive removes, rather than adds, energy beyond a certain amplitude while maintaining the counterclockwise character of the motion.

III. NONLINEAR DYNAMICS OF RESONANT CHIRAL MODE

We now investigate the dynamics of the trimer in a regime where an amplified chiral mode is predicted by the linear theory. Figure 3 shows a numerically integrated trajectory for such a system, initialized in the amplified Floquet mode. Consistent with the linear theory, the mode amplitude grows exponentially at early times, with a rate predicted by the magnitude of the corresponding Floquet multiplier. However, the trajectory eventually deviates from the linear behavior, displaying oscillations in the amplitude that decay to attain a steady

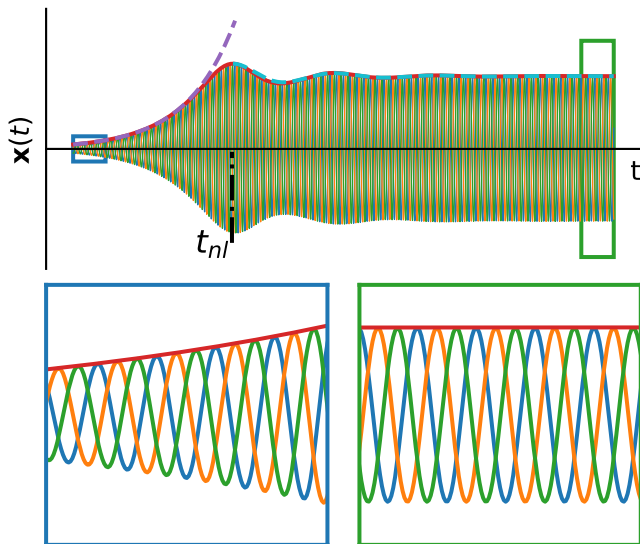


FIG. 3. Numerical solution of the full equations of motion. The parameters are $\epsilon = 0.06$, $\delta = 0.6$, $k = 1$, $\omega = \sqrt{1 + 3k} = 2$, $\gamma = 2\omega = 4$. The system is initialized in its unique amplified Floquet eigenstate, normalized to have magnitude 0.1. The red line shows the amplitude obtained by solving the reduced averaged equations (12). Blue boxes indicate the extents of the insets below. **Top:** The full trace from $t = 0$ to $t = 250$. The purple line is an exponential approximation whose growth rate is obtained from an averaging analysis of Eq. (14) in section III B; the growth rate obtained from this process also matches the perturbative calculation of the amplifying Floquet multiplier for Eq. (14) in [33]. The time t_{nl} marks the transition to nonlinear behavior, also described in Section III B. **Blue inset:** The initial exponential amplification. **Green inset:** The steady state showing chiral motion (each coordinate oscillating out-of-phase by $2\pi/3$). Note that the two insets show the length of time, so the frequencies in each interval can be compared.

amplitude at late times. The insets to Fig. 3 show that the relative phases of the three oscillators in the steady state match the initial phases, confirming that the chirality of the parametrically amplified Floquet mode is preserved in the nonlinear-stabilized steady state. Many parameter regimes exhibit the qualitative features of the trajectory described above. The quantitative details of the trajectory—specifically, the steady-state amplitude and the time scales of the exponential growth, the appearance of the amplitude oscillations, and their eventual decay—vary with the parameters in Eq. (1). These variations can be understood quantitatively using an approximate analysis, which uses the large separation of scales between the oscillation of the individual masses and the slower dynamics of the amplitude and phase of the motion.

Throughout this section, numerical integrations follow procedures described in Appendix B.

A. Averaged equations

In order to understand the long-term dynamics of the trimer model, we use averaging to reduce the equations of motion (1) to an approximate autonomous system [34–36]. This produces results equivalent at first order to the two-variable expansion method of [34, 37], and has been applied previously to analyze slow dynamics of parametric oscillators [7, 21, 24]. To compute the averaged equations, we first express the equations of motion in the general form of weakly nonlinear, weakly coupled oscillators:

$$\ddot{x}_j + x_j + h_j(\vec{x}, \dot{\vec{x}}, t) = 0 \quad (3)$$

Here, $h_j(\vec{x}, \dot{\vec{x}}, t)$ includes the parametric drive, damping, nonlinearity, and coupling terms:

$$h_j(\vec{x}, \dot{\vec{x}}, t) = \delta \cos(\gamma t + \beta_j) x_j + \epsilon \dot{x}_j + x_j^3 + k(2x_j - x_{j+1} - x_{j-1}) \quad (4)$$

We then change coordinates, representing the state of the system in terms of complex, time-dependent amplitudes A_j . The coordinate change is

$$x_j = A_j e^{i\omega t} + \text{c.c.} \quad (5)$$

$$\dot{x}_j = i\omega A_j e^{i\omega t} + \text{c.c.} \quad (6)$$

where c.c. stands for the complex conjugate of all the terms preceding it. The frequency ω is a free parameter that should be chosen to match the expected oscillation frequency in the linear limit. In this case, we will choose $\omega = \sqrt{1 + 3k}$, which is the frequency of the traveling-wave mode of the linearized, non-modulated system.

Equations (5) and (6) can be combined and time-averaged to obtain a single equation for \dot{A}_j in the averaging approximation (see Appendix B, Subsection B 2):

$$\dot{A}_j = \frac{1}{2\omega} i \langle h_j e^{-i\omega t} \rangle + \frac{1 - \omega^2}{2\omega} i A_j \quad (7)$$

Here the arguments x_j and \dot{x}_j to the function h_j are to be expressed in terms of A_j and A_j^* as given by Equations (5) and (6), and angle brackets indicate time averaging over the period $2\pi/\omega$.

We now apply Eq. (7) to the trimer. As explained by the linear Floquet analysis (Sec. II), the chiral modulation singles out the counterclockwise traveling-wave mode for parametric resonance, which occurred within a window of modulation frequencies near 2ω as seen in Fig. 2(d). To examine the resonance window, we set $\gamma = 2\omega + \Delta\gamma$, where $\Delta\gamma$ is a frequency shift with the same order of smallness as the other parameters. Inserting Eq. (4) into Eq. (7), we obtain averaged equations for the amplitude:

$$\begin{aligned} \omega \dot{A}_j &= \frac{1}{4} i \delta A_j^* e^{i(\Delta\gamma t + \beta_j)} \\ &- \frac{1}{2} \omega \epsilon A_j + \frac{3}{2} i |A_j|^2 A_j \\ &+ \frac{1}{2} i k (2A_j - A_{j-1} - A_{j+1}) + \frac{1}{2} i (1 - \omega^2) A_j \end{aligned} \quad (8)$$

Up to this point, the three degrees of freedom oscillate with the same frequency ω , but with different amplitudes and phases encoded in the separate variables A_j . However, the trajectories in Fig. 3 appear to maintain similar amplitudes and oscillation phase differences among the three oscillators at all times. Motivated by this observation, we substitute an ansatz with equal amplitudes separated by $2\pi/3$ in phase:

$$A_j = Ae^{-2\pi i(j-1)/3}, \quad (9)$$

i.e., the amplitude variables are simply offset by a phase of $2\pi/3$ [38]. Under this substitution the three amplitude equations all become the same equation, which we call the reduced equation:

$$\omega \dot{A} = \frac{1}{4}i\delta A^* e^{i\Delta\gamma t} - \frac{1}{2}\omega\epsilon A + \frac{3}{2}i|A|^2 A \quad (10)$$

Equation (10) provides an efficient description of the slow (relative to the oscillation scale ω) dynamics of the chiral motion through a single complex amplitude $A(t)$. Although it describes the motion of all three oscillators at long times, it has the form of the averaged equations of motion of a single nonlinear Mathieu oscillator with damping ϵ , parametric drive δ/ω , and nonlinearity parameter $1/\omega$ (see appendix A for an explanation of the nonlinearity parameter). The solid line in Fig. 3 shows a trace of $|2A(t)|$, the real amplitude of the oscillations, obtained by numerically integrating the reduced equation using the same parameters as the full dynamics. We observe that the reduced equation solution closely follows the envelope of the full dynamics, and captures all the salient features of the amplitude variation over time. For discussion of the correct mathematical interpretation of the averaging method, see Appendix B.

B. Time scales of the motion

We now use the reduced equation to derive the time scales identified previously in the full dynamics of Fig. 3, which describe the transition from growth to ringdown and the subsequent ringdown of the amplitude. Knowing these time scales allows us to estimate convergence times for the amplitude, which lets us identify an additional boundary in parameter space distinguishing damped trimers—i.e., those for which the amplitude will converge within the period of interest—from effectively undamped trimers, which exhibit persistent oscillations that can be traced to a conserved quantity in the dynamics. (By “effectively undamped,” we mean that the time scale of interest is much smaller than the time scale of the amplitude’s decay due to damping.)

1. Initial amplitude growth rate

We begin by deriving the initial growth rate of the amplitude. For this section it will be helpful to express the

reduced equation for the complex amplitude A , Eq. (10), in terms of the real amplitude r and real phase offset c obtained via

$$A = \frac{r}{2}e^{ic} \quad (11)$$

Specializing to the resonance case ($\Delta\gamma = 0$), the reduced equation then transforms into the two coupled equations

$$\begin{aligned} \dot{r} &= \frac{\delta}{4\omega}r \sin(2c) - \frac{1}{2}\epsilon r \\ \dot{c} &= \frac{\delta}{4\omega} \cos(2c) + \frac{3}{8\omega}r^2 \end{aligned} \quad (12)$$

Equations (12) constitute an autonomous, planar, nonlinear system for the averaged amplitude r and phase offset c .

The exponential growth phase of the motion can be understood by removing the r^2 term from (12) to obtain

$$\begin{aligned} \dot{r} &= \frac{\delta}{4\omega}r \sin(2c) - \frac{1}{2}\epsilon r \\ \dot{c} &= \frac{\delta}{4\omega} \cos(2c) \end{aligned} \quad (13)$$

Since the r^2 term arises from the cubic nonlinearity in the original equations of motion, this is a good approximation when the amplitude of the motion is small, and amounts to linearizing the original equations of motion before averaging.

However, the equations (13) are also the result of averaging the following damped, *linear* Mathieu equation [37]:

$$\ddot{x} + \left(1 + \frac{\delta}{\omega} \cos 2t\right)x + \epsilon\dot{x} = 0 \quad (14)$$

If we apply the coordinate change $x(t) = r(t) \cos(t + c(t))$, $\dot{x}(t) = -r(t) \sin(t + c(t))$ and time-average over a time interval of length 1, we obtain Eq. (13). This shows that we can understand the behavior of the reduced averaged equations (13) through the “un-averaged” equation (14).

To determine the exponential growth rate of the amplitude, however, it is more convenient to average the “un-averaged” equation (14) using a coordinate change that results in linear averaged equations. One such coordinate change is

$$x = a \cos t + b \sin t \quad (15)$$

$$\dot{x} = -a \sin t + b \cos t \quad (16)$$

Inserting this coordinate change into (14) and time-averaging over an interval of length 1 produces the following linear equation:

$$\begin{bmatrix} \dot{a} \\ \dot{b} \end{bmatrix} = \begin{bmatrix} -\epsilon/2 & -\delta/(4\omega) \\ -\delta/(4\omega) & -\epsilon/2 \end{bmatrix} \begin{bmatrix} a \\ b \end{bmatrix} \quad (17)$$

We can extract the growth rate from this linear system. The solutions to this system are

$$\begin{aligned} a &= \frac{1}{2}(a_0 + b_0)e^{-\frac{1}{2}(\epsilon + \frac{\delta}{2\omega})t} + \frac{1}{2}(a_0 - b_0)e^{-\frac{1}{2}(\epsilon - \frac{\delta}{2\omega})t} \quad (18) \\ b &= \frac{1}{2}(a_0 + b_0)e^{-\frac{1}{2}(\epsilon + \frac{\delta}{2\omega})t} - \frac{1}{2}(a_0 - b_0)e^{-\frac{1}{2}(\epsilon - \frac{\delta}{2\omega})t} \end{aligned}$$

where $a_0 = a(0)$ and $b_0 = b(0)$. As long as $\delta/(2\omega) > \epsilon$, the exponent in the $a_0 - b_0$ terms will be positive and the amplitude will diverge exponentially. We will see from Eq. (32) that this is also the condition for a fixed point of the amplitude to exist in the nonlinear system.

Thus, for the first part of the motion when oscillations are being amplified from their initial value, we expect the amplitude to exponentially diverge with a growth constant of $\frac{1}{2}(\frac{\delta}{2\omega} - \epsilon)$. This is consistent with the perturbative analysis of the linear Mathieu equation in [37]. Agreement between the expected exponential rise and the actual amplification is shown in Fig. 3.

2. Transition to nonlinear behavior

We can estimate the time scale at which the exact solution starts to deviate from the exponential growth of the linear system by equating the amplitude of the exponentially growing linear solution to a length scale X_s derived from the nonlinearity. Let g be the exponential growth constant for the linear system, so that the amplitude is

$$a(t) = a_0 e^{gt} \quad (19)$$

We find that the time scale t_{NL} at which the behavior of the trimer deviates from its linear counterpart is

$$t_{NL} = \frac{1}{g} \ln \frac{X_s}{a_0} \quad (20)$$

This time is plotted in Fig. 3 as a vertical line. To compute t_{NL} for the figure, we use the exponent of the growing mode in equations (18), ie

$$g = \frac{1}{2} \left(\frac{\delta}{2\omega} - \epsilon \right) \quad (21)$$

For X_s , we use the dimensionful nonlinearity parameter α derived from the dimensionful equations of motion. Before nondimensionalization, the nonlinearity in the equation of motion for oscillator j has the form αx_j^3 , where α is a constant with dimensions of (length)⁻². We therefore set

$$X_s = \frac{1}{\sqrt{\alpha}} \quad (22)$$

See Appendix A for a detailed description of the nondimensionalization procedure and the parameter α .

3. Amplitude ringdown

Once the amplitude stops growing exponentially, it undergoes decaying oscillations around a fixed point. The dynamics of these oscillations can be mapped to a damped harmonic oscillator by linearizing around the fixed point. We let

$$s = r - r_* \quad (23)$$

$$q = c - c_* \quad (24)$$

where r_* and c_* are the coordinates of the fixed point obtained by setting $\dot{r} = 0$ and $\dot{c} = 0$ in Eq. (12) (see Eq. (32)).

To first order in s and q , the equations of motion for these variables are

$$\begin{bmatrix} \dot{s} \\ \dot{q} \end{bmatrix} = \begin{bmatrix} 0 & (\delta r_*/(2\omega)) \cos(2c_*) \\ 3r_*/(4\omega) & -\epsilon \end{bmatrix} \begin{bmatrix} s \\ q \end{bmatrix} \quad (25)$$

By differentiating the equation for q , these can be further simplified to a single equation:

$$\ddot{q} + \epsilon \dot{q} + \left[\left(\frac{\delta}{2\omega} \right)^2 - \epsilon^2 \right] q = 0 \quad (26)$$

Therefore, the ringdown to the steady amplitude shows damped oscillations with natural frequency

$$\Omega_{rd} = \sqrt{(\delta/(2\omega))^2 - \epsilon^2} \quad (27)$$

and damping constant $\epsilon/2$; i.e. the oscillations die out over a time that scales as $1/\epsilon$. The dashed cyan curve in Fig. 3 shows a damped oscillation obeying Eq. (26), shifted to begin at the peak of the amplitude oscillations and having an amplitude equal to the difference between the peak amplitude and the fixed point amplitude.

C. Undamped system: persistent amplitude oscillations

From the linearized analysis of the previous section, the convergence time of the amplitude goes to infinity when the damping ϵ goes to zero; i.e., the amplitude never converges to a steady state. In this case, the reduced averaged equations predict amplitude oscillations with a well-defined period that persist forever, retaining memory of the initial conditions indefinitely. We now analyze these persistent oscillations and verify their existence in the full dynamics of the system.

Upon setting $\epsilon = 0$ and $\Delta\gamma = 0$, the reduced averaged equations (12) admit a conserved quantity

$$C = \frac{br^4 + 2ar^2 \cos(2c)}{16b} \quad (28)$$

where $a = \delta/(4\omega)$ and $b = 3/(8\omega)$ (see Appendix C for a derivation) [39]. In the resonance case, the reduced dynamics confines the system to move along the level

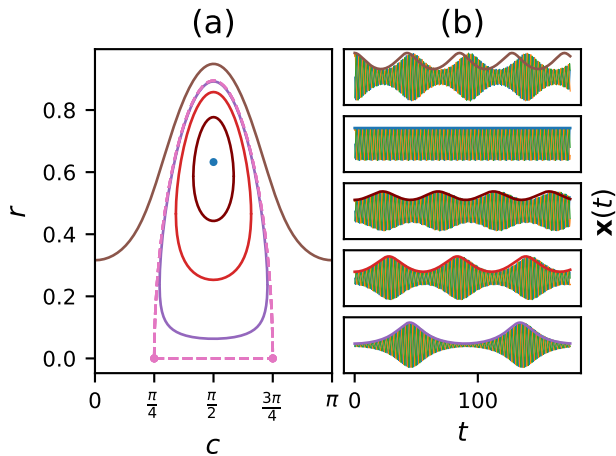


FIG. 4. (a): Phase portraits of the reduced averaged equations computed from the conserved quantity. The initial conditions for the amplitude index the different curves; the phase is initialized at the fixed point value. (b): Numerical solutions to the full equations of motion compared to the amplitude found by solving the reduced averaged equation. The colors of the amplitudes correspond to the colors of the phase curves in the left figure. The vertical range shown in the plots at right is $-1.1 \leq x_j \leq 1.1$. As the system moves deeper into the nonlinear regime (higher amplitudes), the averaging approximation should break down; this may explain the deviation between the averaged and exact trajectories at the top of the right figure. The parameter values are $\epsilon = 0$, $\delta = 0.6$, $k = 1$, $\gamma = 2\omega = 2\sqrt{1 + 3k} = 4$.

curves of C in phase space with value set by the initial conditions, so we can find r as a function of c from the expression for C . Level curves for a sampling of C values are shown in Fig. 4(a). We find that the phase space is divided into two regions: one where level curves close around a finite-amplitude fixed point

$$(r_*, c_*) = \left(\sqrt{\frac{2\delta}{3}}, \frac{\pi}{2} \right) \quad (29)$$

and one with open curves that wrap around the phase direction. These regions are separated by two heteroclinic orbits connecting two unstable, zero-amplitude fixed points (dashed pink lines and pink dots, respectively, in Fig. 4(a)). The fixed points are at $\pi/4$ and $3\pi/4$ on the c -axis; the heteroclinic orbits are the segment of the c -axis between the fixed points and the downward-opening curve whose equation (derived in Appendix C) is

$$r = \sqrt{-\frac{2a}{b} \cos(2c)}. \quad (30)$$

Physically, all reduced trajectories away from the fixed points and the separatrix display amplitude oscillations over a finite range of values specified by C . The phase also oscillates for the closed curves, whereas it advances monotonically over the trajectory for the open curves (see

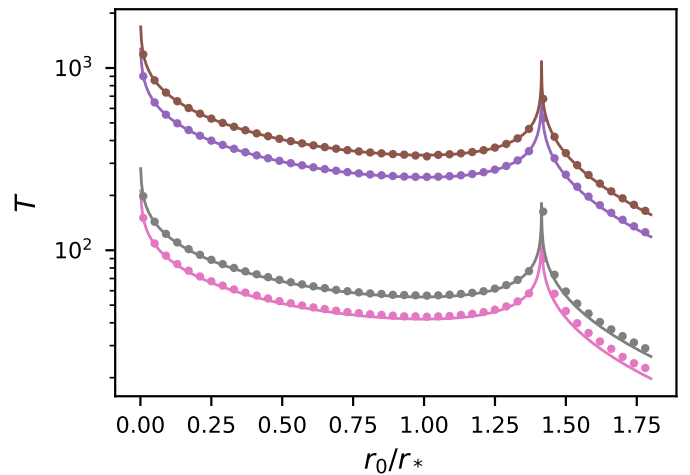


FIG. 5. Comparison of the integral expression for the trimer period (Equations (C16) and (C22), solid lines) with periods extracted from numerical integration of the dynamical equations. Each curve corresponds to a different set of system parameters, and each position on the horizontal axis represents the initial value (alternatively, a different level curve of the conserved quantity). Solid curves show the period predicted by the integral expression and dots show the numerically-computed period. The parameters are $k = 1, \delta = 0.1$ (purple); $k = 2, \delta = 0.1$ (brown); $k = 1, \delta = 0.6$ (pink); $k = 2, \delta = 0.6$ (gray). All traces have zero damping (i.e., $\epsilon = 0$). See Appendix B for a detailed description of the methods used to generate this figure.

thick solid curves in Fig. 4(b) for representative $r(t)$ trajectories, and Fig. C10 for both variables). As a result of the phase variable having a component that increases linearly in time, the fast oscillations for initial conditions corresponding to the open curves experience an effective frequency shift, which we derive in Appendix C. Trajectories initialized exactly at the nonzero fixed point (Eq. (29)) display a steady amplitude (blue trajectory in Fig. 4).

The conserved quantity and its associated orbits are derived from the reduced equations of motion. To compare these dynamics to the dynamics of the full equations of motion, we generated initial conditions for all three oscillators for a given initial (r, c) pair using the ansatz Eq. (9) and numerically evaluated the resulting trajectories from Eq. (1). The full trajectories largely follow the expectation from the averaged trajectories (Fig. 4(b)): the high-frequency oscillations of the three trimers maintain $2\pi/3$ phase offsets while experiencing slow amplitude variations that closely track the predicted $r(t)$, but with a lag that is most visible for the trajectory corresponding to an open orbit.

To quantify the discrepancy between the full dynamics and the reduced trajectories, we compared the time period of the amplitude oscillations in the full trajectories to the predicted period of the closed orbits in the reduced phase space, which is given by the expression (derived in

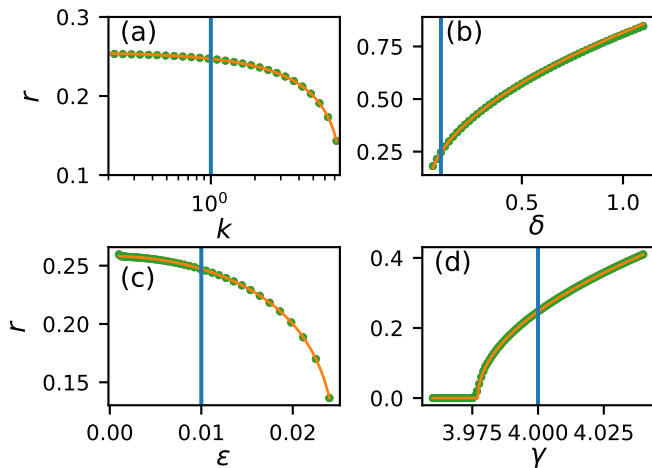


FIG. 6. Comparison of steady-state amplitudes of numerical traces with the analytical prediction from averaging theory. Numerically-computed amplitudes from full trimer trajectories are shown as dots. In each panel, one parameter is varied while the other parameters are kept fixed at the baseline values indicated by vertical blue lines: $\epsilon = 0.01$, $\delta = 0.1$, $k = 1$, $\gamma = 2\omega = 2\sqrt{1 + 3k} = 4$. Orange curves shows the prediction from averaging theory for the amplitude, Eq. (34). Away from resonance, Eq. (35) predicts a finite-amplitude fixed point for $\gamma > 3.97708$.

Appendix C)

$$T = \frac{2}{aB} K\left(\frac{B^2 - 1}{B^2}\right) \quad (31)$$

where $K(m)$ is the complete elliptic integral of the first kind [40] and $B = \frac{4b}{a}\sqrt{-C}$ is a positive real constant. There is a similar expression for the open curves—Eq. (C23)—also derived in Appendix C. Figure 5 compares the predicted time period to periods extracted from numerical integrations at different initial conditions. The period of the motion diverges as the system's trajectory approaches the heteroclinic orbits, as predicted by the integral result and confirmed by the nonzero singularity in the figure.

D. Damped system: robust chiral steady state

Now we consider the case when the damping ϵ is nonzero, and show that the constant-amplitude chiral steady state, reached for a particular instance in Fig. 3, is a feature of the motion over wide ranges of parameters and initial conditions. When $\Delta\gamma = 0$, the reduced equations Eq. (12) admit the fixed point (r_*, c_*) given by

$$\sin 2c_* = \frac{2\omega\epsilon}{\delta}, \quad r_* = \sqrt{\frac{2}{3}} \left[\delta^2 - (2\omega\epsilon)^2 \right]^{1/4} \quad (32)$$

This is the only stable fixed point of the reduced averaged equations with a nonzero amplitude. When $\epsilon = 0$, we recover the nonzero fixed point from the undamped motion,

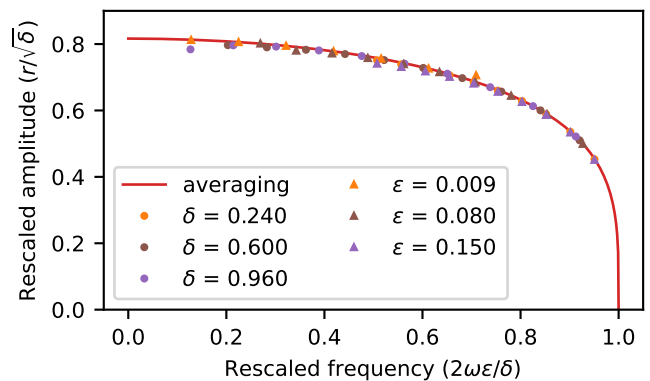


FIG. 7. Rescaled trimer steady-state amplitude from numerical integration of the full dynamics (symbols) as a function of rescaled frequency. Under these rescalings, the fixed-point amplitude predicted by averaging theory, Eq. (32), becomes a universal function (solid curve). Different markers correspond to different combinations of the parameters δ and ϵ . For the markers with varied δ , ϵ is fixed at 0.06, and for the markers with varied ϵ , $\delta = 0.6$. For each (δ, ϵ) combination, the rescaled frequency is varied by changing k .

Eq. (29). Damping transforms the fixed point from a nonlinear center into an attractor [34]. Numerical investigation of the phase portraits generated by Eq. (12) suggested that all trajectories in the reduced system eventually reach this unique attractor when there is positive nonzero damping. We hypothesize that all initial conditions in the 2D phase plane of the reduced averaged equations eventually flow to the fixed point so long as $r(0) > 0$.

This suggests that in the full trimer dynamics, there is an open set of initial conditions that flows to an attractor corresponding to the fixed point of the reduced averaged equations. To test this hypothesis, we numerically integrated the full dynamical equations of the trimer after initializing the system in the amplified Floquet mode with an overall magnitude of 0.1 while varying system parameters (see Appendix B). On resonance ($\Delta\gamma = 0$), the full dynamics converged to the predicted fixed point over wide ranges of system parameters, as shown by comparing the amplitude extracted from numerical trajectories (symbols) to the prediction of Eq. (32) (curves) in Fig. 6(a–c). The form of Eq. (32) shows that the dependence on the various parameters at resonance can be captured by a single rescaled frequency variable $\omega_{rs} = 2\omega\epsilon/\delta$, provided the amplitude is rescaled as $r_{rs} = r_*/\sqrt{\delta}$. We confirm this universal dependence in Fig. 7, where we show that numerically-computed steady-state amplitudes for a variety of parameters collapse onto a single curve $r_{rs} = \sqrt{2/3}(1 - \omega_{rs}^2)^{1/4}$. We also verified that the trimer oscillation phases match the expectation of consistent $2\pi/3$ offsets (Appendix D).

Away from resonance—i.e., when $\Delta\gamma \neq 0$ —the reduced equation no longer admits a fixed point. However, it does admit a state in which the amplitude r is fixed

and the phase offset c changes linearly with time. Setting $c = c_0 + c_1 t$, substituting into Eq. (10), and setting $\dot{A} = 0$, we obtain

$$c_1 = \frac{\Delta\gamma}{2}, \quad \sin(2c_0) = \frac{2\omega\epsilon}{\delta} \quad (33)$$

for the phase and

$$r_* = \sqrt{\frac{4\omega\Delta\gamma}{3} + \frac{2}{3}\sqrt{\delta^2 - (2\omega\epsilon)^2}} \quad (34)$$

for the amplitude. This result suggests that systems away from resonance also approach a chiral steady state with constant amplitude, as long as the (signed) frequency shift is above the threshold for r_* to be real:

$$\Delta\gamma_{\min} = -\frac{1}{2\omega}\sqrt{\delta^2 - (2\omega\epsilon)^2} \quad (35)$$

Numerical trajectories of the full trimer system away from resonance (Fig. 6(d)) also agree with these predictions: the trimer attains a steady-state amplitude predicted by Eq. (34) for modulation frequencies above a threshold set by Eq. (35).

The averaging result Eq. (34) states that the steady-state amplitude grows as $\sqrt{\Delta\gamma}$. This would appear to be at odds with Fig. 2(d), which shows that the Floquet multipliers only exceed unity for a finite range of frequencies. We show the linear frequency response can be understood as a limit of the nonlinear response in Appendix E.

Our analysis of the reduced system under damping has uncovered a fixed point determined by the system parameters, which describes a chiral constant-amplitude steady state that the reduced system appears to reach from any initial condition in the reduced (r, c) phase space. (This is in contrast to the undamped system, where the fixed point still exists but it is not an attractor and memory of the initial conditions persists in the periodic orbits.) Our numerical results in figures 6 and 7 provide evidence that the full system, when initialized in a space-time symmetric state, reliably settles in the constant-amplitude chiral steady state regardless of its initial rescaled amplitude. However, the presence of an attractor in the reduced phase space introduces the possibility that the chiral steady state is also an attractor for initial conditions that deviate from the amplified Floquet mode, as long as they are in the neighborhood of the known attractor. While a full stability analysis of the coupled nonlinear parametric system is beyond the scope of this work (but see Appendix F for a perturbative investigation of the weak-coupling limit), we numerically investigate the convergence of the full trimer system to the chiral steady state. See Appendix G for the relationship of the averaged trajectories to the exact trajectories in the presence of a fixed point.

We solved the system with initial conditions sampled randomly from the 6-dimensional phase space of the full dynamics. We chose these initial conditions at increasing

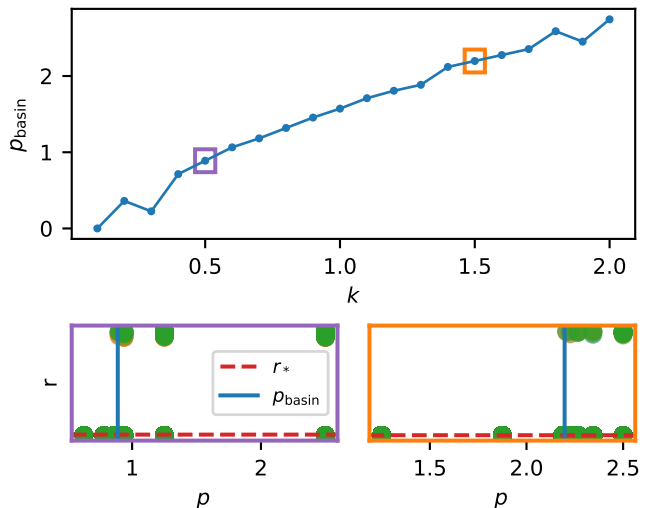


FIG. 8. Phase space radius p_{basin} of the basin of attraction of the amplitude r_* in Eq. (32) as a function of the coupling k . This plot is evidence of an open set of initial conditions around the fixed point that converge to the fixed-point amplitude. Each radius is found by a binary search procedure in which initial conditions a set phase space distance away from the fixed point are generated, and the trimer is integrated from those initial conditions. The inset panels below the figure show the convergence of the search to the determined phase-space radius (blue vertical lines) for the two points indicated by boxes in the top panel. The red horizontal line in the lower panels shows the fixed point amplitude r_* . The basin radius is determined by finding the largest possible radius such that every initial condition on a sphere of that radius around the fixed point converges to the expected amplitude r_* . For this plot, we tested 300 random initial conditions per phase space radius. Integrations for this plot used the parameters $\delta = 0.6$, $\epsilon = 0.06$, and fixed the modulation frequency γ at $\gamma = 2\omega$ with $\omega = \sqrt{1 + 3k}$. The k -values used are on the x-axis of the plot and range from 0.1 to 2 in increments of 0.1.

Euclidean distances away from a point on the manifold corresponding to the the fixed point of the reduced dynamics (see Appendix H for details). We define a radius of convergence in phase space, p_{basin} , as the largest initialization distance from this point at which all sampled trajectories converged to oscillatory steady states with the predicted amplitude r_* . Since inter-oscillator coupling is essential to single out the chiral state from other steady states with different phase relationships expected at zero or weak coupling (see Appendix F), we expect that the convergence to the chiral state should increase with coupling constant k .

Results for a range of couplings in the vicinity of the baseline value $k = 1$, with other parameters kept constant, are shown in Fig. 8. We observed a non-zero radius of convergence for all except the smallest values of coupling, confirming that the fixed point amplitude is reached from a broad range of initial conditions. The radius increases with coupling strength in accordance with our expectation. For the linearized system, since the chi-

ral mode is the only exponentially growing mode, it always dominates at long times regardless of the initial conditions; our numerical results suggest that the chiral nonlinear steady state also possesses a degree of robustness as it is attained from a range of initial conditions.

Our analysis in this subsection establishes the main conclusion of this work: a chiral constant-amplitude steady state is obtained in the trimer for a wide range of parameters and initial conditions. The steady state arises from a confluence of selective amplification of one of the traveling-wave modes through phase-controlled parametric amplification, stabilization of the amplified mode through nonlinearity, exchange of energy among resonators through coupling, and loss of initial conditions through damping. The fixed point position predicted from the *reduced* averaged equations, Eq. (32), successfully predicts the steady-state amplitude of the *full* dynamics as long as the initial conditions lie within basins of attraction whose size is determined by the coupling strength. To establish the relevance of this non-trivial nonlinear parametric state to experiments, we next show that it can be achieved in a realistic continuum model of coupled plate resonators.

IV. SIMULATION OF CHIRAL STEADY STATE IN COUPLED PLATE RESONATORS

Nonlinear parametric oscillators model complex dynamics in a variety of mechanical, optical, and electronic systems [22, 41–46]. The essential ingredients are: distinguishable oscillator degrees of freedom that can be coupled, whose natural frequency (corresponding to the effective stiffness) can be modulated in time, and which have a harmonic response at small amplitudes with a stiffening anharmonic response that becomes significant at larger amplitudes. Elastic plate microresonators [43, 47–49] provide an attractive platform with all these ingredients present, which can, in principle, be scaled up to large numbers of resonators using semiconductor fabrication techniques [50–52]. In isolated resonators, the continuum out-of-plane deflections form a ladder of eigenmodes with discrete frequencies at the level of linear response; one of these eigenmodes (typically the lowest-frequency, or fundamental, mode) serves as an individual oscillator degree of freedom localized to the resonator. Small connecting regions between resonators provide mechanical couplings among these discrete degrees of freedom. The modulation of the effective stiffness is realized by changing the in-plane tension in the plate through electrostatic [46, 53, 54] or thermal [55] means, which changes the natural frequency of the modes (akin to tuning a drum). The geometric nonlinearity inherent to plate mechanics ensures a nonlinear response for large out-of-plane oscillations, even when the constituent material remains in the linear elastic regime.

To establish the feasibility of observing nonlinear-stabilized chiral parametric oscillations, we performed

finite-element simulations of a trimer of coupled plate resonators with the required chiral modulation. Details of the model and its implementation are provided in Appendix I. The trimer consists of three triangular plates with overlapping corners (Fig. 9(a)), which are modeled as thin plates with isotropic linear elasticity and clamped boundary conditions along the external and internal edges. Each resonator is subjected to a uniform in-plane bulk stress with components

$$\sigma_{xx} = \sigma_{yy} = \sigma_0 \left[1 + \delta' \cos \left(\Gamma t + \frac{2\pi}{3} j \right) \right], \quad (36)$$

where Γ is the modulation frequency and j indexes the resonators, to recreate the effect of a chiral modulation of the in-plane tension on the resonators. The effect of damping in the system was recreated by adding a dissipative component to the elastic moduli.

When $\delta' = 0$, the lowest three modes in a linear eigenmode analysis of the assembly can be interpreted as coupled modes arising from the fundamental mode on each resonator (Fig. 9(b)). The lowest-frequency mode involves all resonators vibrating in-phase, whereas the next two modes are nearly degenerate and involve out-of-phase combinations of the fundamental modes, consistent with the linear eigenmode analysis of the static discrete model (compare to Fig. 1). We set up a space-time parametric modulation of the membrane tensions following Eq. (36), setting $\Gamma = 2\omega_1$ to parametrically excite the counterclockwise traveling wave. Since the numerical eigenfrequency analysis of the continuum system provides an arbitrary linear superposition of the degenerate clockwise and counter-clockwise propagating modes as the latter modes in Fig. 9(b), we are not able to initialize the system purely in the resonant mode. Instead, we initialized the system in the second linear eigenmode, ensuring some overlap of the initial condition with the desired counterpropagating mode. We tracked the vertical displacements of the centroids of the three colored regions as proxies for the states of the fundamental mode oscillations within each plate resonator.

Results of a dynamical simulation with space-time modulation strength $\delta' = 0.1$ are shown in Fig. 9(c). At this modulation, the system shows an initial transient around $2\mu\text{s}$ long, after which the three resonators oscillate at roughly $2\pi/3$ out of phase, consistent with the counterclockwise traveling wave. Subsequently, the trajectory tracks the expected evolution of the counterclockwise traveling wave as predicted by the discrete model, including an exponentially growing phase followed by ring-down oscillations that decay toward a finite-amplitude chiral steady state (compare to the discrete model trajectories of Fig. 3). This numerical result shows that tension-modulated micromechanical systems provide the essential ingredients of dynamic control, coupling, and nonlinearity necessary to harbor the chiral steady states established in this work. We further used fits to our analytical results in the different stages of the motion to fix parameters of the discrete model (see

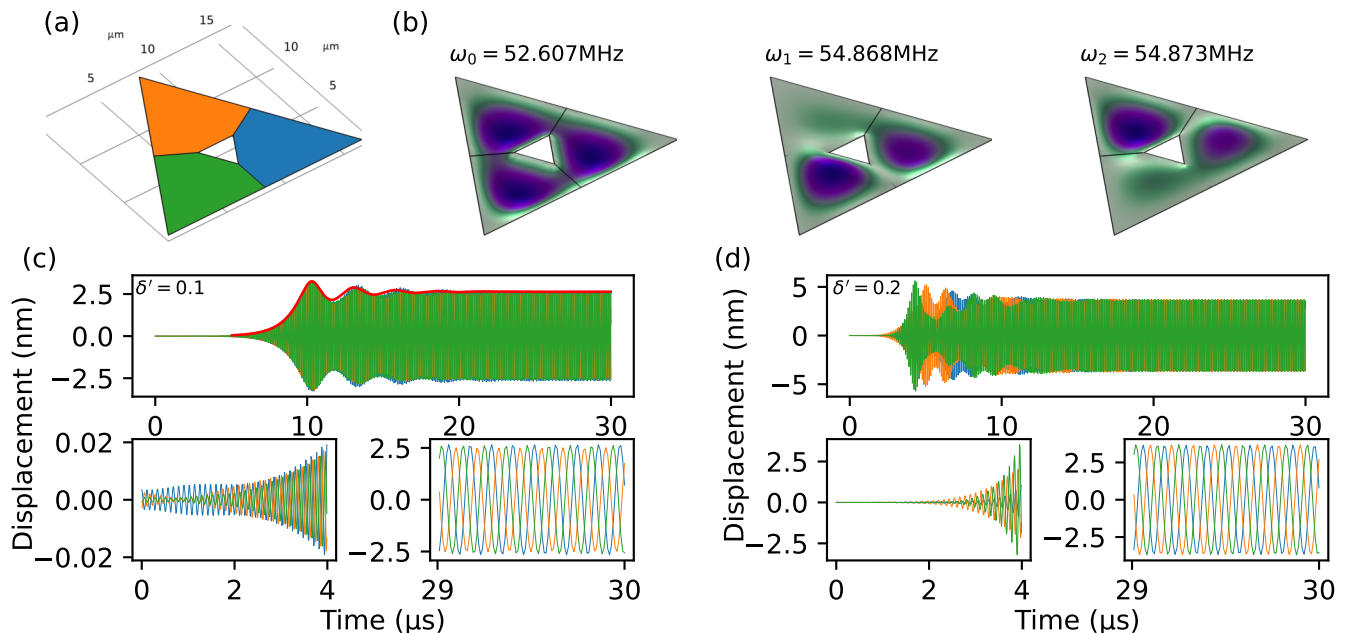


FIG. 9. Chiral steady states in a continuum model of mechanical parametric oscillators. (a) Trimer of plate resonators arranged in a triangle. Black lines delineate three regions within which the in-plane stresses are modulated with the same phase offsets as in the discrete model (colors indicate modulation phase as in Fig. 1). (b) Eigenmodes of the static system with lowest three eigenfrequencies. The second and third eigenfrequencies differ by a fraction of less than 10^{-4} . The next eigenfrequency is well-separated at $\omega_3 = 76.67$ MHz. (c) Numerical time-evolution of vertical displacements at the centroids of the three resonators under space-time modulation of in-plane stresses with $\delta' = 0.1$. Lower panels show zoomed regions at the initial and final stages of the simulation. Red curve shows numerical integration of the reduced averaged equations with parameters extracted as described in Appendix J. (d) Same as (c) but at a higher modulation strength $\delta' = 0.2$.

Appendix J for a detailed description of the fitting procedure), enabling us to predict the amplitude evolution from the reduced model equations (Eq. (10)). The resulting trace (thick red curve in Fig. 9(c)) closely follows the amplitude evolution from the continuum simulations, showing that our discrete model can quantitatively predict the time-evolution of the parametrically amplified mode in a continuum system.

In Sec. III D, we showed that the chiral steady state was reached for a wide range of initial conditions, even if they do not satisfy the strict relative oscillation phases of the ansatz used to generate the reduced averaged equations. We also observed this scenario in the continuum model simulations, as exemplified by the trajectory shown in Fig. 9(d) for a simulation with $\delta' = 0.2$. At this stronger pumping, the initial evolution from the arbitrary member of the degenerate traveling-wave mode subspace quickly deviated from the counterclockwise traveling-wave mode, favoring one resonator over the other two. However, the resonator amplitudes begin to even out during the ringdown phase ($5 \mu\text{s}$ – $15 \mu\text{s}$) which ends with the system reaching a constant-amplitude chiral steady state with the phase offsets corresponding to the counterclockwise traveling mode. The simulation shows that the chiral steady state can be reached at late times even if the trajectory does not follow the traveling-wave ansatz at early times, illustrating the robustness of the chiral

steady state.

V. CONCLUSIONS

We have demonstrated that a ring of coupled nonlinear parametric oscillators with chiral phase-controlled parametric modulation robustly converges to a constant-amplitude chiral steady state over wide ranges of parameters and initial conditions. The modulation was chosen to generate a single unstable Floquet mode in the linearized system whose existence was dictated by space-time symmetry [26]; the steady state in the nonlinear dynamics arises from the stabilization of this mode, showing that nonlinearity can tame Floquet instabilities while maintaining desirable symmetries. The nonlinear evolution of the unstable mode in six-dimensional phase space is well-described by an averaged equation for a *single* nonlinear Mathieu oscillator [7], allowing us to generate analytical predictions for the parameter dependence of the steady state and the time scales dictating the approach to it. In the undamped limit, the system exhibits persistent amplitude oscillations [24] with periods that differ drastically from the NPO frequencies themselves, whose existence is explained by a conserved quantity in the reduced dynamics that identifies two distinct classes of trajectories analogous to librations and rotations. We

tested these predictions against numerical evaluation of the NPO dynamics, and showed that analogous features occur in full-wave simulations of a continuum system of mechanical plate resonators.

While the reduction to a single oscillator assumes a specific form for the dynamics, many aspects of the chiral steady states also persist for dynamical trajectories that are initialized away from the chosen form. At the level of individual oscillators, the steady state is stabilized by a specific phase relationship between the motion and the underlying parametric modulation that balances parametric gains and losses [7, 56], but this leads to $2^3 = 8$ limit cycles, or four possible relative phase relationships, for three decoupled NPOs. Our analysis shows that under sufficiently strong inter-oscillator coupling, these distinct limit cycles collapse to a single relative phase assignment corresponding to the chiral mode. We numerically confirmed that the chiral steady state possess a finite basin of attraction in the expanded six-dimensional phase space, whose radius grows with the coupling strength, showing that the chiral state can be robustly reached without fine-tuning of initial parameters. The validation of our results in simulations of a continuum mechanical system suggests that the stable chiral states could be attainable in a wide variety of coupled NPO systems including optical parametric oscillators [13, 57], nonlinear electrical circuits [22, 24], MEMS systems [43, 46, 51, 52], and Faraday waves [56].

The reduction of the trimer dynamics to a single averaged equation generalizes to rings of any odd number of oscillators with the same space-time symmetry. Since the underlying linear dynamics harbors a chiral amplified mode for all such rings [26], the dimensional reduction suggests a broader principle: space-time symmetric modulation may organize arbitrarily large rings to effectively single-mode nonlinear chiral dynamics, with potential implications for nonreciprocal signal processing [58, 59]. We will investigate this principle in forthcoming work. More broadly, our work highlights modulation phase control as an underutilized tool to sculpt many-body nonlinear steady states in coupled parametric oscillator networks.

ACKNOWLEDGMENTS

Research reported in this publication was supported by the National Science Foundation through award CMMI-2128671. We thank Benjamín Alemán, Brittany Carter, and Uriel Hernandez for insights on the experimental system and for input on parameter values for the plate resonator simulations. Initial layouts of the finite-element model of plate resonators were developed by Brevin Tuttle. We acknowledge useful discussions with Arnaud Lazarus, Abhijeet Melkani, Jason Murphy, and Wenqian Sun. Abhijeet Melkani originated the idea of estimating the nonlinear time scale t_{NL} in Sec. III B, and Wenqian Sun found the elliptic function expressions for the pe-

riod of the conservative trimer amplitude in Eq. (31) and Appendix C.

APPENDIX A: Nondimensionalizing the equations of motion

In terms of dimensionful quantities, the equations of motion for the “trimer” model shown in Fig. 1 are

$$MX_i'' + EX_i' + M\Omega^2(1 + \delta \cos(\Gamma T + \beta_i))X_i \quad (\text{A1})$$

$$+ AX_i^3 + K(2X_i - X_{i-1} - X_{i+1}) = 0 \quad (\text{A2})$$

Here, M is the mass of each oscillator, E is the damping constant, Ω is the natural frequency of the vertical springs, A is the nonlinearity parameter, K is the coupling constant, δ is the parametric drive strength (already dimensionless), Γ is the parametric drive frequency, X_i is the displacement of the i th oscillator, and T is the time. Primes denote differentiation with respect to T , and capital letters are all dimensionful quantities.

If we let $t = \Omega T$ and let a dot denote differentiation with respect to t , we get

$$\ddot{X}_i + \frac{E}{M\Omega} \dot{X}_i + (1 + D \cos(\frac{\Gamma}{\Omega}t + \beta_i))X_i \quad (\text{A3})$$

$$+ \frac{A}{M} X_i^3 + \frac{K}{M} (2X_i - X_{i-1} - X_{i+1}) = 0 \quad (\text{A4})$$

This prompts the definition of the dimensionless quantities

$$\epsilon = \frac{E}{M\Omega}, \quad \gamma = \frac{\Gamma}{\Omega}, \quad k = \frac{K}{M\Omega^2} \quad (\text{A5})$$

and the quantity

$$\alpha = \frac{A}{M\Omega^2} \quad (\text{A6})$$

which has units of $1/(\text{length})^2$.

In terms of these quantities, the equations of motion have the form

$$\ddot{X}_i + \epsilon \dot{X}_i + (1 + \delta \cos(\gamma t + \beta_i))X_i \quad (\text{A7})$$

$$+ \alpha X_i^3 + k(2X_i - X_{i-1} - X_{i+1}) = 0$$

While not fully dimensionless, these equations demonstrate an important feature of oscillator equations with a cubic nonlinearity: since the nonlinearity parameter α has units of $1/(\text{length})^2$, choosing a value of the nonlinearity α is equivalent to choosing a length unit. This means that if we have a solution obtained for a particular value of α , there exists a family of solutions that are related to the known solution by a rescaling of the positions and velocities. It also means that if we would like to study the effect of changing the strength of the nonlinearity on the solutions for a given set of initial conditions, this is equivalent to varying the magnitudes of the initial conditions while holding α constant.

To obtain the fully dimensionless equations (1) used in the main text, we define the length scale $X_s = 1/\sqrt{\alpha}$. We then define dimensionless displacements x_i via $X_s x_i = X_i$ to obtain the dimensionless equations of motion (1).

APPENDIX B: Methods

1. Computing trajectories

We numerically integrated the trimer equations of motion using the `solve_ivp` function in SciPy [60]. We used the default RK4 integrator with a relative tolerance of 10^{-6} and an absolute tolerance of 10^{-9} when computing damped trajectories, and relative and absolute tolerances of 10^{-7} and 10^{-10} , respectively, when computing undamped trajectories.

2. Derivation of the general averaged complex amplitude equation (7)

Here we derive the general equation (7). First, differentiate Eq. (6) to obtain

$$\ddot{x}_j = i\omega \dot{A}_j e^{i\omega t} - \omega^2 A_j e^{i\omega t} + \text{c.c.} \quad (\text{B1})$$

and insert this result into Eq. (3) to obtain

$$\left[(1 - \omega^2) A_j e^{i\omega t} + i\omega \dot{A}_j e^{i\omega t} + \text{c.c.} \right] + h_j = 0 \quad (\text{B2})$$

Next, add the two coordinate change equations (5)–(6) to find

$$\frac{1}{2} \left(x_j - i \frac{\dot{x}_j}{\omega} \right) = A_j e^{i\omega t} \quad (\text{B3})$$

Differentiate Eq. (5), insert it into this result, and cancel like terms to find that $A_j e^{i\omega t}$ is purely imaginary:

$$\Re\{A_j e^{i\omega t}\} = 0 \quad (\text{B4})$$

Write this result as

$$\dot{A}_j e^{i\omega t} - \text{c.c.} = 2\dot{A}_j e^{i\omega t} \quad (\text{B5})$$

Putting this last result (B5) into (B2) and isolating \dot{A}_j , we obtain

$$\dot{A}_j = \frac{1}{2\omega} i h_j e^{-i\omega t} + \frac{1 - \omega^2}{2\omega} i (A_j + A_j^* e^{-2i\omega t}) \quad (\text{B6})$$

Under the coordinate change equations (5)–(6), this equation is exactly true for any system that obeys Eq. (3).

Finally, time-averaging both sides over a period $2\pi/\omega$, we obtain Eq. (7). When averaging, we treat the amplitudes A_j as constants and assume $\langle dA_j/dt \rangle \approx d\langle A_j \rangle/dt$, approximations that hold as long as h_j is sufficiently small [35].

3. Analysis of conserved quantity (Fig. 5)

Here, we derive the expressions Eq. (C17) and Eq. (C23) for the period in terms of the complete elliptic

integral of the first kind, starting from their respective integral expressions Eq. (C16) and Eq. (C22). We use the following convention for the complete elliptic integral of the first kind, after [40]:

$$K(m) = \int_0^1 \frac{dv}{\sqrt{(1-v^2)(1-mv^2)}} \quad (\text{B7})$$

Eq. (C17) can be derived from Eq. (C16) by making the substitution

$$v = \sqrt{\frac{u^2 - B^2}{1 - B^2}} \quad (\text{B8})$$

After factoring $1/B$ from the integrand in Eq. (C22), Eq. (C23) is already in the form of $K(m)$ with $m = -1/B^2$.

Finally, we note that as described in the main text, the period approaches π/a as $B \rightarrow 0$, consistent with the linearization around the fixed point. This can be seen by evaluating the elliptic integral Eq. (C17) when $B = 0$:

$$T \rightarrow \frac{2}{a} K(0) = \frac{2}{a} \int_0^1 \frac{dv}{\sqrt{1-v^2}} = \frac{\pi}{a} \quad (\text{B9})$$

Whenever we numerically evaluated elliptical integrals, we used the function `ellipk` from the the SciPy Python library's special functions module, `scipy.special`.

4. Determining the period of a numerical integration (Fig. 5)

To extract the period of the amplitude oscillations from numerical trimer trajectories (Fig. 5, dots), we computed the upper envelope of the trajectory, used a Butterworth filter to remove high-frequency features, and computed the time between the adjacent local maxima of the filtered envelope. The smallest of the time intervals between adjacent local maxima over the trajectory was reported as the numerical period; this choice prevented errors due to missed maxima in the peak-finding algorithm.

5. Parameter sweeps in Sec. III D

For the integrations where the system parameters were varied (Figures 6 and 7), we varied the system parameters k , δ , ϵ , and γ one at a time around a set of baseline parameters. When each parameter was varied, the others were kept at their baseline values, with the exception that when k was varied, the modulation frequency γ was also varied such that $\gamma = 2\omega$ unless otherwise specified. For numerical experiments that varied one of the system parameters, the system was initialized in the unique amplified Floquet eigenstate of the linearized system (the system (1) without the cubic term), rescaled to have a norm of 0.1, except in cases where random initial conditions were chosen. The Floquet eigenstate depends on the parameters.

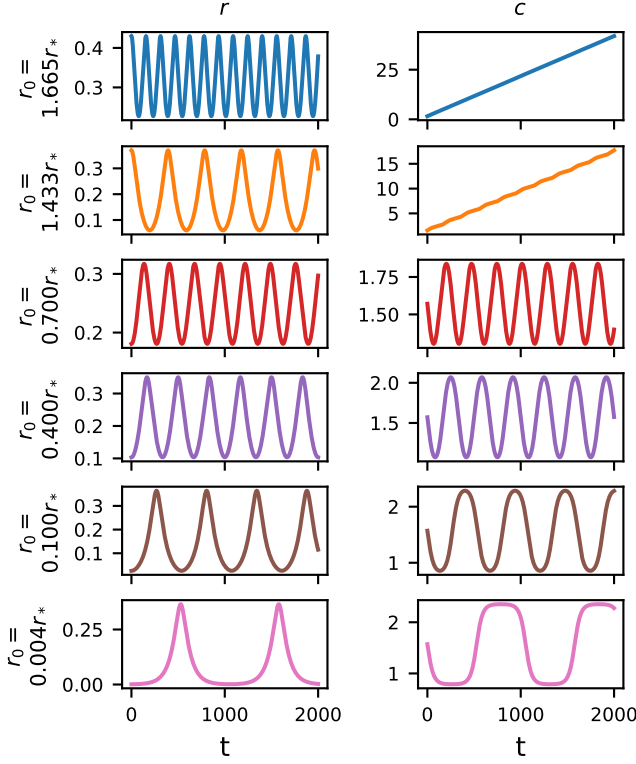


FIG. C10. Amplitude r (left column) and phase offset c (right column) trajectories for the reduced averaged equations at different initial conditions. The initial conditions for each curve were $c(0) = \pi/2$ and $r(0)$ as stated at the left of the amplitude plot, where r_* is the fixed point amplitude. Note that for the first two curves, the initial conditions are in the “open” region of the phase space (the phase curves do not close around the fixed point) and for the remainder of the curves, the initial conditions are in the “closed” region (the phase portraits close around the fixed point). The curves in the “open” region experience a linear-in-time phase shift that corresponds to a frequency shift in the trajectories of the trimer coordinates, in addition to a periodic phase modulation. The curves in the “closed” region experience a periodic phase modulation, but their corresponding trimer trajectories experience no frequency shift.

In all trials, the steady-state amplitude was estimated from the numerical integrations of Eq. (1) by taking the maximum value of each oscillator’s position in an interval close to the end of the integration time. For Fig. 6, this interval was the last 200 dimensionless time units of the 10000-unit integration window. For Fig. 7, the interval was also the last 200 dimensionless time units, but the total integration time was 2000 units because the amplitude was observed to converge more quickly for these parameters.

APPENDIX C: Conserved quantity in undamped motion

In this section, we will derive the equations for the level curves of the conserved quantity C ; we will also derive the period of the amplitude variation and the equations of the heteroclinic orbits in Fig. 4, which we refer to as the separating curve because it separates open and closed orbits. Note that in the subsequent analysis, all functions of c are periodic with period π and have mirror symmetry over the c -axis, so we consider the phase space as having a half-cylinder topology with r running along the length of the cylinder and c running around its perimeter. The curves that close around the nonzero fixed point will be called “closed” and those that do not will be called “open”, even though—strictly speaking—they close around the perimeter of the cylindrical phase space.

Recall that the reduced averaged equations on resonance and without damping are

$$\begin{aligned} \dot{r} &= \frac{\delta}{4\omega} r \sin(2c) \\ \dot{c} &= \frac{\delta}{4\omega} \cos(2c) + \frac{3}{8\omega} r^2 \end{aligned} \quad (\text{C1})$$

where r is the amplitude of the oscillations and c is the phase offset. Let $a = \frac{\delta}{4\omega}$ and $b = \frac{3}{8\omega}$. The quantity

$$C = \frac{br^4 + 2ar^2 \cos(2c)}{16b} \quad (\text{C2})$$

is a constant of the motion.

We can see this by computing $\frac{dC}{dt}$ and using Eq. (C1):

$$\begin{aligned} \frac{dC}{dt} &= \frac{\partial C}{\partial r} \dot{r} + \frac{\partial C}{\partial c} \dot{c} \\ &= \left(\frac{r^3}{4} + \frac{ar^2}{4b} \cos(2c) \right) \left(ar \sin(2c) \right) \\ &\quad + \left(-\frac{ar^2}{4b} \sin(2c) \right) \left(a \cos(2c) + br^2 \right) \\ &= 0 \end{aligned} \quad (\text{C3})$$

Having established C as a conserved quantity, we can now rearrange the expression for C to compute r as a function of c . This yields

$$r = \pm \sqrt{-\frac{a}{b} \cos(2c) \pm \sqrt{\frac{a^2}{b^2} \cos^2(2c) + 16C}} \quad (\text{C5})$$

The positive and negative values of r are not physically distinct, so we neglect the root where the outer (\pm) is ($-$) and take

$$r = \sqrt{-\frac{a}{b} \cos(2c) \pm \sqrt{\frac{a^2}{b^2} \cos^2(2c) + 16C}} \quad (\text{C6})$$

For closed curves around the nonzero fixed point, the inner (\pm) distinguishes between upper and lower halves

of the trajectory. For open curves, the root with the inner (\pm) taken to be ($-$) is imaginary, and only the ($+$) root yields a real amplitude.

Next, we can use the expression for the amplitude Eq. (C6) and the equation for \dot{c} to determine the period of the closed oscillations. Substitute Eq. (C6) into the equation for \dot{c} to obtain

$$\begin{aligned} \frac{dc}{dt} &= a \cos(2c) + br^2 \\ &= \pm \sqrt{a^2 \cos^2(2c) + 16b^2 C} \end{aligned} \quad (\text{C7})$$

Consistent with what was previously claimed, the inner (\pm) from Eq. (C6) indexes the upper and lower halves of the closed curves, since \dot{c} will be positive on one half of the trajectories and negative on the other half. For this system, since the state moves clockwise around the curves, $\dot{c} > 0$ on the upper half of the trajectory and $\dot{c} < 0$ on the lower half. We also see that the sign of C determines whether or not a closed orbit will exist, because if $C > 0$, there is no value of c for which $\dot{c} = 0$. Therefore, we must have that $C < 0$ on closed orbits and $C > 0$ on open orbits.

Knowing this, we proceed first with computing the period for the closed orbits, which have $C < 0$. Separate the variables in Eq. (C7) to obtain

$$dt = \frac{dc}{\pm \sqrt{a^2 \cos^2(2c) + 16b^2 C}} \quad (\text{C8})$$

To find the period, we need to integrate Eq. (C8) over one full orbit. Let c_- and c_+ be the points on the orbit where $\dot{c} = 0$; these points will define the limits of integration. In one orbit, the system starts at $c = c_+$, follows the lower half of the trajectory to $c = c_-$, and then follows the upper trajectory back to $c = c_+$. Let t_0 , t_1 , and t_2 be the times at which the orbit begins at c_+ , reaches c_- , and returns to c_+ , respectively. Then the period is the integral of dt over these time intervals:

$$\begin{aligned} T &= \int_{t_0}^{t_1} dt + \int_{t_1}^{t_2} dt \\ &= \int_{c_+}^{c_-} \frac{dc}{-\sqrt{a^2 \cos^2(2c) + 16b^2 C}} \\ &\quad + \int_{c_-}^{c_+} \frac{dc}{\sqrt{a^2 \cos^2(2c) + 16b^2 C}} \\ T &= \frac{2}{a} \int_{c_-}^{c_+} \frac{dc}{\sqrt{\cos^2(2c) - B^2}} \end{aligned} \quad (\text{C9}) \quad (\text{C10})$$

where we have introduced the positive real constant

$$B = \frac{4b}{a} \sqrt{-C} \quad (\text{C11})$$

A straightforward calculation shows that $B = 1$ at the nonzero fixed point (32). Also, since $C > 0$ for open

curves and $C < 0$ for closed curves, $C = 0$ at the ‘‘separating curve’’ that separates the open curves from the closed curves. We will later show this curve to be a union of two heteroclinic orbits joining two unstable fixed points. By the definition above, B also equals 0 at this separating curve.

Now we need to find the turning points c_- and c_+ . Set $dc/dt = 0$ and use Eq. (C7) to obtain

$$\cos(2c) = \pm \frac{4b}{a} \sqrt{-C} = \pm B \quad (\text{C12})$$

Modulo π , there are 4 solutions to this equation; they are

$$c = \{c_0, \pi/2 - c_0, \pi/2 + c_0, \pi - c_0\} \quad (\text{C13})$$

where

$$c_0 = \frac{1}{2} \cos^{-1}(B) \quad (\text{C14})$$

The solutions c_0 and $\pi - c_0$ result in values of C that are greater than 0, which we previously established cannot be true for closed curves. Therefore the turning points occur at

$$c_{\pm} = \frac{\pi}{2} \pm \frac{1}{2} \cos^{-1}(B) \quad (\text{C15})$$

With these limits and the substitution $u = \cos(2c)$ the integral Eq. (C10) becomes

$$T = \frac{2}{a} \int_B^1 \frac{du}{\sqrt{(u^2 - B^2)(1 - u^2)}} \quad (\text{C16})$$

(Note that the transformation $u = \cos(2c)$ must be applied carefully since the expression for dc in terms of u differs on the intervals $[c_-, \pi/2]$ and $[\pi/2, c_+]$. We have $2dc = \pm du/\sqrt{1 - u^2}$, with ($-$) for c in $[c_-, \pi/2]$ and ($+$) for c in $[\pi/2, c_+]$. Failing to consider this may result in a transformed integral with identical lower and upper limits.)

Finally, Eq. (C16) can be rewritten in terms of the complete elliptic integral of the first kind, $K(m)$ [40]:

$$T = \frac{2}{aB} K\left(\frac{B^2 - 1}{B^2}\right) \quad (\text{C17})$$

From the analysis of the linearized equations around the nonzero fixed point, we expect from Eq. (27) that as the phase curves approach the fixed point, the periods of the phase curves will approach the value obtained in the linearized analysis, namely

$$T_{\text{lin}} = \frac{1}{\Omega} = \frac{\pi}{a} \quad (\text{C18})$$

The elliptic integral $K(m)$ approaches $\pi/2$ as $m \rightarrow 0$, so from Eq. (C23), $T \rightarrow \pi/a$ as $B \rightarrow 1$. See Appendix B for derivations of Eq. (C23) and its limit as $B \rightarrow 1$.

Next, we compute the period of the open phase curves. For these phase curves there are no turning points where

$\dot{c} = 0$, so $C > 0$. Starting from Eq. (C8) with $C > 0$, we proceed similarly to the previous case. We define a new constant

$$\mathcal{B} = \frac{4b}{a}\sqrt{C} = -iB \quad (\text{C19})$$

and with this definition (C8) becomes

$$dt = \frac{2}{a} \frac{dc}{\sqrt{\cos^2(2c) + \mathcal{B}^2}} \quad (\text{C20})$$

Because there are no turning points, the curves travel the entire length of the cylindrical phase space in one period; therefore the limits of integration for finding the period are 0 and π . A derivation similar to that of the closed-curve period produces

$$T = \frac{1}{a} \int_{-1}^1 \frac{du}{\sqrt{(u^2 + \mathcal{B}^2)(1 - u^2)}} \quad (\text{C21})$$

Since the integrand is even, we can rewrite this as

$$T = \frac{2}{a} \int_0^1 \frac{du}{\sqrt{(u^2 + \mathcal{B}^2)(1 - u^2)}} \quad (\text{C22})$$

which makes it more obvious that this expression will approach the result of the closed-curve expression near the separating curve. As with the closed curves, the period in this case can be written in terms of the elliptic integral $K(m)$:

$$T = \frac{2}{a\mathcal{B}} K\left(-\frac{1}{\mathcal{B}^2}\right) \quad (\text{C23})$$

As previously stated, since $C > 0$ for open curves and $C < 0$ for closed curves, the curve separating the open curves from the closed curves must have $C = 0$. Using this, we can derive an expression for the separating curve. Setting $C = 0$ in (C6) and taking the positive solution for r we obtain as solutions either

$$r = \sqrt{-\frac{2a}{b} \cos(2c)} \quad (\text{C24})$$

or

$$r = 0 \quad (\text{C25})$$

These two curves intersect at the unstable fixed points given by

$$c = \frac{\pi}{4}, r = 0 \text{ and } c = \frac{3\pi}{4}, r = 0 \quad (\text{C26})$$

The segment between $c = \pi/4$ and $c = 3\pi/4$ and the curve given by (C24) form two heteroclinic orbits, orbits that start and end at the unstable fixed points and take infinite time to complete.

The separation of the phase space into regions with closed and open phase curves has two salient physical consequences for the original trimer model that are valid

in the averaging approximation. The first is that if the system begins in a state close to the separating curve, the period of the amplitudes and phases of the fast oscillations will be large, and will diverge as initial conditions are chosen progressively closer to the separating curve.

The second consequence is less obvious. For initial conditions inside the separating curve, the phase portraits of the amplitude r and phase offset c will be closed and the fast oscillations of the trimer will have a phase that oscillates periodically around a constant value. For initial conditions outside the separating curve, however, the phase offset c will increase monotonically. The result is that the corresponding fast oscillations of the trimer will experience a frequency shift in addition to a periodic modulation of their phases.

To see why this is the case, first consider the closed phase curves. Because these curves close around a point in the phase space, we have that the net change in c over one period T of the slow variables is zero. Therefore

$$\int_0^T \dot{c} dt = 0 \quad (\text{C27})$$

i.e., \dot{c} has zero mean. The integral of a periodic function with zero mean is a periodic function, so we conclude that $c(t)$ is periodic with period T .

Now consider the open phase curves. Using the definition of the parameter \mathcal{B} (C19), we can rewrite Eq. (C7) as

$$\dot{c} = a\sqrt{\cos^2(2c) + \mathcal{B}^2} \quad (\text{C28})$$

(only the positive root is physical; see the discussion below Eq. (C6)). This function has a minimum of $a\mathcal{B}$ and a maximum of $a\sqrt{1 + \mathcal{B}^2}$, both of which are positive, so its mean is positive and we can write

$$\dot{c} = \langle \dot{c} \rangle + \dot{c}_{ZM} \quad (\text{C29})$$

where $\langle \dot{c} \rangle$ is the time average of \dot{c} over one period T (a constant) and \dot{c}_{ZM} is a periodic function with zero mean. Integrating this form of \dot{c} we obtain

$$c(t) = c(0) + \langle \dot{c} \rangle t + \int_0^t \dot{c}_{ZM}(s) ds \quad (\text{C30})$$

The last integral in the expression above is T -periodic, so we conclude that the phase offset includes a constant term, a linearly-increasing term, and a periodic term. The linearly increasing term is responsible for the frequency increase. See Fig. C10 for example amplitude and phase trajectories for open and closed curves.

APPENDIX D: Chirality of the system at various parameter values and initial conditions

Chirality is another feature of the trajectories of the trimer system that first-order averaging predicts. Here,

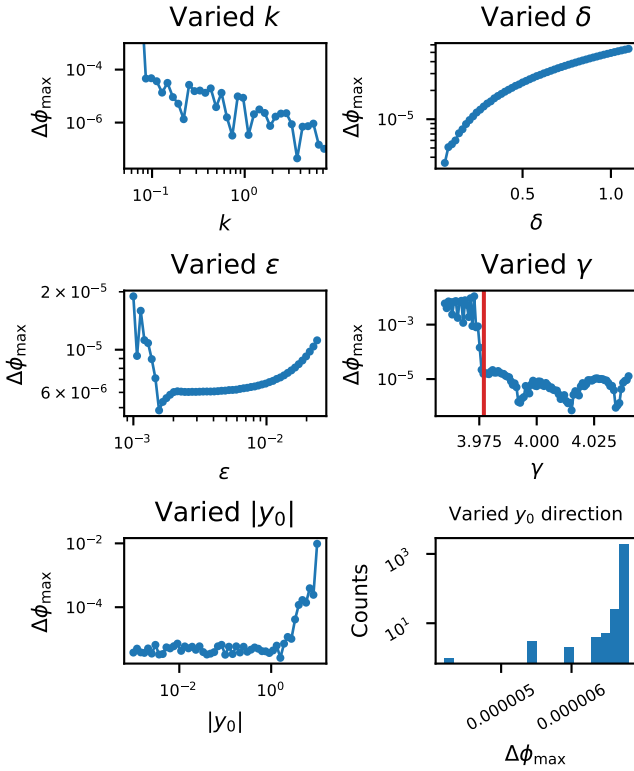


FIG. D11. $\Delta\phi_{\max}$ parameter at different values of the system parameters. $\Delta\phi_{\max}$ is a measure of the largest possible deviation from $2\pi/3$ phase spacing given the values of the traces at long times. In the top four plots, the baseline initial conditions (amplified Floquet eigenstate scaled to magnitude 0.1) are used and three of the four parameters k, ϵ, δ , and γ are held fixed; the varied parameter is indicated in the title, and for the parameters that are fixed, the values are $\epsilon = 0.01$, $\delta = 0.1$, $k = 1$, and $\gamma = 2\omega = 2\sqrt{1+3k} = 4$. In the lower left plot, these parameter values and the baseline initial conditions are used, but the magnitude of the initial condition vector is varied. In the lower right plot, the baseline parameters are used and the magnitude of the initial condition vector is fixed at 0.1, but the direction of the initial condition vector is chosen randomly from the surface of a sphere in the phase space. The chiralities resulting from a sample of 2000 randomly-chosen initial conditions are plotted as a histogram. For the varied k , varied ϵ , and varied y_0 direction plots, the integration interval was $[0, 10000]$; for the varied δ , γ , and $|y_0|$ plots the interval was $[0, 2000]$. The last 1000 points of the time traces were sampled to compute the chirality. In the varied γ plot, parametric amplification only occurs for γ values greater than the value at the red line.

“chirality” means a breaking of mirror symmetry in the trajectories.

Chirality presents in the trimer system as oscillations that peak and fall in a definite order and with definite relative phases. We define a chirality parameter \mathcal{C} to

measure the chirality:

$$\mathcal{C}(\phi_1, \phi_2, \phi_3) = \left| \left\langle \sum_{j=1}^3 e^{i\phi_j} \right\rangle \right| \quad (\text{D1})$$

where ϕ_j is the phase of the complex amplitude A_j of the j th oscillator as defined in Eq. (5) and Eq. (6). Brackets denote averaging over a time interval that occurs after the trajectories have approximately reached a steady amplitude. With this definition, the chirality is zero if the three phases are separated by $2\pi/3$. Note that a chirality parameter *greater than zero* corresponds to a motion in which the oscillator phases are *not* evenly spaced.

The physical significance of this parameter is not obvious for nonzero values, so we further define a geometric parameter $\Delta\phi_{\max}$. If three phases ϕ_1, ϕ_2 , and ϕ_3 make the sum $|\sum_{j=1}^3 e^{i\phi_j}|$ equal to M , and we are given that ϕ_2 and ϕ_3 are $2\pi/3$ and $4\pi/3$, respectively, the value of ϕ_1 is given by

$$\cos \phi_1 = \frac{2 - M^2}{2} \quad (\text{D2})$$

Motivated by this observation, we define $\Delta\phi_{\max}$ via

$$\cos \Delta\phi_{\max} = \frac{2 - C^2}{2} \quad (\text{D3})$$

$\Delta\phi_{\max}$ is a proxy for the largest possible deviation from evenly-spaced phases. Plots of $\Delta\phi_{\max}$ for various values of the system parameters $k, \epsilon, \delta, \gamma$, as well as different values of the initial conditions, are shown in Fig. D11. For each plot, the maximum $\Delta\phi_{\max}$ is less than approximately 0.01, and for most parameter values shown $\Delta\phi_{\max} < 10^{-4}$, showing that the phases remain very close to evenly spaced at long times.

APPENDIX E: Linear frequency response as a limit of the nonlinear response

As described in Sec. II, Floquet theory predicts that the linearized trimer will experience exponentially amplifying oscillations that continue to grow for all time as long as the modulation frequency γ lies within a particular range. This range is the interval of frequencies where the Floquet multipliers exceed 1 in magnitude and is shown in Fig. 2(d) for a particular set of parameter values. But in Fig. 6(d), the steady-state amplitude continues to grow even when γ leaves the amplified region shown in Fig. 2(d). This would appear to be inconsistent with Floquet theory, since in the nonlinear model amplified states are accessible even when the modulation frequency exceeds the maximum amplified frequency. While we do not fully explain the system’s amplification outside the frequency window Floquet theory predicts, in this appendix we show that the response of the linear system can be understood as a zero-nonlinearity limit of the nonlinear response.

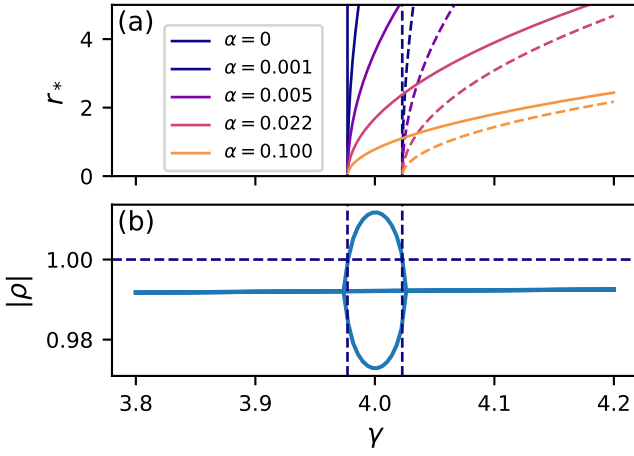


FIG. E12. In the limit of zero nonlinearity, the stable and unstable steady-state amplitude curves collapse onto the boundaries of the Floquet amplification region. (a): The stable steady-state amplitudes r_* (solid lines) and unstable steady-state amplitudes \tilde{r}_* (dashed lines) at varied nonlinearity α . (b): The Floquet multipliers of the trimer. Vertical dashed lines are the bifurcation frequencies γ_- and γ_+ where the stable and unstable fixed points emerge, respectively. The horizontal line is $|\rho| = 1$. Note that the vertical lines intersect $|\rho| = 1$ exactly where the Floquet multipliers equal 1 in magnitude, indicating that the bifurcation frequencies obtained via averaging mark the boundaries of the amplification window obtained via Floquet theory.

We first restore the dimensionful nonlinearity parameter α in the equations of motion (see Appendix A). This parameter represents the strength of the nonlinearity, with larger α corresponding to a stronger nonlinearity. With α restored, the steady-state amplitude in Eq. (34) becomes

$$r_* = \sqrt{\frac{4\omega\Delta\gamma}{3\alpha} + \frac{2}{3\alpha}\sqrt{\delta^2 - (2\omega\epsilon)^2}} \quad (\text{E1})$$

Provided $\Delta\gamma$ is sufficiently large, the same expression with a minus sign in front of the second term also produces a real root, which we label \tilde{r}_* :

$$\tilde{r}_* = \sqrt{\frac{4\omega\Delta\gamma}{3\alpha} - \frac{2}{3\alpha}\sqrt{\delta^2 - (2\omega\epsilon)^2}} \quad (\text{E2})$$

The amplitude r_* corresponds to a stable constant-amplitude state, and \tilde{r}_* to an unstable one. [7]

Let

$$\Delta\gamma_* = \frac{1}{2\omega}\sqrt{\delta^2 - (2\omega\epsilon)^2} \quad (\text{E3})$$

From Eq. (E1), the minimum frequency at which the stable fixed amplitude r_* exists is $\gamma_- = 2\omega - \Delta\gamma_*$. Similarly, from Eq. (E2) the minimum frequency at which the unstable amplitude \tilde{r}_* exists is $\gamma_+ = 2\omega + \Delta\gamma_*$. Applying Floquet theory to the Mathieu equation Eq. (14) says

that the steady-state amplitude of the linear trimer is infinity for $\gamma_- < \gamma < \gamma_+$ and zero otherwise.[33] In short, these bifurcation frequencies of the nonlinear trimer correspond to the limits of the amplification window of the linear trimer. In the limit as the nonlinearity α goes to zero, we would therefore expect the response function of the trimer to go to two vertical lines at γ_+ and γ_- . From equations (E1) and (E2), the stable and unstable steady-state amplitudes do converge to these vertical lines in this limit, in the sense that for any $r > 0$ and $\epsilon > 0$ we can choose an $\alpha > 0$ such that the maximum frequency deviation of the r_* and \tilde{r}_* curves from $2\omega \pm \Delta\gamma_*$ is less than ϵ . This is illustrated in Fig. E12. While this does not explain the presence of amplification in the region outside $[\gamma_-, \gamma_+]$, it shows consistency between the linear and nonlinear frequency responses in the appropriate limit.

APPENDIX F: Perturbative theory of the small- k fixed points

At small coupling k , a new set of fixed points emerge that we can account for using a perturbative expansion of the averaged equations.

First, we motivate why we might expect more fixed points to exist. By applying the averaging methods of the section stating the fixed point formula, it is straightforward to show that Eq. (32) also applies to a single, decoupled nonlinear Mathieu oscillator if we set $\omega = 1$. Eq. (32) is also π -periodic in the phase c , meaning that within the range of phases $[0, 2\pi)$, there are actually two physically distinct phases, differing by π , that yield a solution. (While it may appear that Eq. (32) admits four fixed points in this range, two of them are nonphysical as they lead to imaginary values of the amplitude.)

When the trimer is completely decoupled, these considerations of an independent Mathieu oscillator would indicate that there are actually eight fixed points accessible to the system, one for each choice of the phases of the three oscillators. Since the phase of the parametric drive determines the phases of the fixed points, and the phase of the parametric drive differs by $2\pi/3$ between adjacent oscillators, the phase spaces of the oscillators are identical except for a displacement of $2\pi/3$ in the phase direction. This means that the fixed points can have phases that differ by $2\pi/3$ or by $\pi/3$ in the limit of zero coupling, depending on the choice of each individual oscillator's phase.

We could conjecture from this that if we introduce a very small coupling in the trimer, there would still be a set of fixed points with phase spacing at or near $\pi/3$, and that these fixed points would persist as we increase the coupling until a bifurcation occurred. Theory and numerical experiments, which we present next, support the existence of these small- k , near- $\pi/3$ -spaced fixed points.

To derive the perturbative expressions for these fixed points, we insert an ansatz with approximately $\pi/3$ -spaced phases into equation (8) and expand to first-

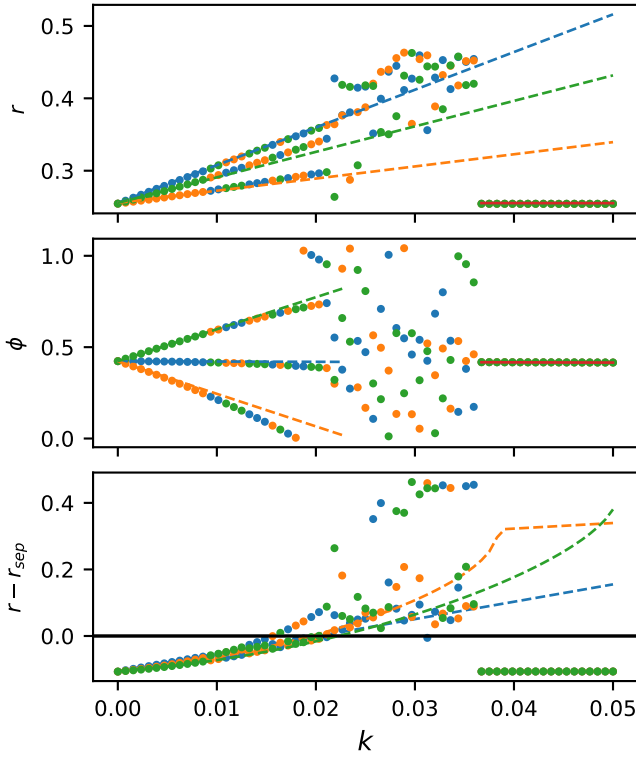


FIG. F13. Perturbation theory of the small- k fixed points. **First two rows:** Steady-state amplitudes r and phases ϕ of the trimer as functions of the coupling k at small values of k . Each color indicates a different oscillator. The perturbation theory predictions are dashed lines; numerical results are lines with circular markers. The red line is the prediction for the $2\pi/3$ -spaced fixed point. In the second plot, the phases are shown mod $\pi/3$. For small values of k , the amplitudes and phases agree with perturbation theory up to cyclic permutations of the indices. Past a threshold k value they diverge from the prediction, and past another threshold k value, the system converges to the $2\pi/3$ -spaced fixed point discussed in the main text. **Third row:** The difference between the numerical and perturbative amplitudes and the amplitude of the separatrix at the corresponding phase value. Dots show the differences in numerical amplitudes from the separatrix, and dashes show the perturbation theory differences from the separatrix. The divergence from perturbation theory occurs roughly at the value of k where the numerical and perturbative amplitudes cross the separatrix. Parameters used are $\epsilon = 0.01$ and $\delta = 0.1$; the modulation frequency γ was varied with k so that $\gamma = 2\sqrt{1+3k}$. The integration time interval was $[0, 5000]$.

order in k . We start by rearranging Eq. (8). Letting $a = \delta/(4\omega)$, $b = 3/(8\omega)$, $g = k/(2\omega)$, and $U = -\epsilon/2 + i[k/\omega + (1 - \omega^2)/(2\omega)]$, we have

$$(4b|A_j|^2 - iU)A_j + ae^{i\beta_j}A_j^* - gi(A_{j-1} + A_{j+1}) \quad (\text{F1})$$

Here, as before, $\beta_j = 2\pi(j-1)/3$ with $j \in \{1, 2, 3\}$ and index arithmetic understood to be mod 3 (e.g., $j+3 = j$).

Into this we substitute the ansatz

$$\begin{aligned} A_1 &= \frac{r_1}{2}e^{ic_1} & (\text{F2}) \\ A_2 &= \frac{r_2}{2}e^{i(c_2+\pi/3)} \\ A_3 &= \frac{r_3}{2}e^{i(c_3-\pi/3)} \end{aligned}$$

In this ansatz, we take r_j and c_j to be perturbed by the coupling k relative to their values when $k = 0$. In other words, we take

$$\begin{aligned} r_j &= r + ks_j & (\text{F3}) \\ c_j &= c + kd_j \end{aligned}$$

where r and c are solutions to the averaged fixed-point equation for a single, decoupled nonlinear Mathieu oscillator, which are the values given in Eq. (32) with $\omega = 1$. Inserting Eq. (F2) with Eq. (F3) into Eq. (F1), setting the time derivatives to zero, multiplying through by ω , and expanding to first order in k , we arrive at three equations. The terms in these equations that are order 0 in k cancel, since they reproduce the fixed point equation for an isolated nonlinear Mathieu oscillator.

From the terms proportional to k (order 1 in k), we obtain three decoupled equations of the form

$$C(s_j, d_j) = D_j \quad (\text{F4})$$

where $C(s, d)$ is given by

$$\begin{aligned} C(s, d) &= \frac{\delta}{4}e^{-2ic}(-ird + s) & (\text{F5}) \\ &+ \frac{1}{8}\left[(-4r + 6ir\epsilon) + (9r^2 + 4i\epsilon)s + (3ir^2 - 4r\epsilon)d\right] \end{aligned}$$

and D_1 , D_2 , and D_3 are

$$D_1 = r \cos(\pi/3) \quad (\text{F6})$$

$$D_2 = -ir \sin(\pi/3) \quad (\text{F7})$$

$$D_3 = ir \sin(\pi/3) \quad (\text{F8})$$

From Eq. (F4), we can obtain a linear equation in the two perturbation variables s_j and d_j by equating the real and imaginary parts on either side. Solving this equation for each value of j and multiplying by k gives the perturbations to the decoupled fixed points.

As stated previously, there are eight fixed points possible at zero coupling owing to the two phase choices available to each oscillator. Two of these result in steady-state oscillations with phase differences of $2\pi/3$ between adjacent oscillators, and six result in $\pi/3$ phase spacing. In this analysis we have chosen an ansatz (F2) that assumes the steady-state phases will be close to one particular zero-coupling configuration: i.e., the configuration with oscillator 1 at zero relative phase, with oscillator two ahead by $\pi/3$ and oscillator 3 behind by $\pi/3$. While this is only one of six possible choices, the other choices can be obtained by a combination of cyclically permuting

the indices and displacing all phases by π . These choices will all result in the same set of steady-state amplitudes and phases, with the only change between choices being which oscillator converges to which amplitude and phase, and possibly an overall π phase difference in all three steady-state phases.

In Fig. F13, we compare the values of the predicted fixed points to steady-state values obtained via numerical integration. The figure shows good agreement between the numerical results and the perturbative prediction until a threshold value of k , at which point the perturbation theory breaks down. This breakdown corresponds roughly to the value of k at which the fixed points cross the separatrix between open and closed curves in the phase space projections for each oscillator.

While we do not discuss them here in detail, in our numerical investigations we found other steady states that exhibit regularity of some kind without having amplitudes and phases that converge (for example, steady states that appear to be combinations of two harmonics). At points in the phase space and parameter space that are far from where we have investigated, we expect that the variety of behaviors accessible to this system at long times is richer than what we have described in this work. Nonetheless, we emphasize that in the neighborhood of parameter space focused on in the main text, the system appears to converge robustly to the $2\pi/3$ -spaced fixed point over a wide range of initial conditions.

APPENDIX G: Mathematical interpretation of the averaging method

Having found a fixed point of the reduced averaged equations, we comment on the mathematical interpretation and implications of results obtained by averaging. The averaged equations are “approximations to Eq. (1)” in the sense that they are guaranteed to have solutions that remain close to the corresponding solutions of Eq. (1) for a time scale determined by the size of the parameters, with larger parameters leading to a smaller time scale [35]. We have analytically found a fixed point of the reduced averaged equations, which corresponds to a fixed point of the averaged equations, and the numerical evidence presented in Sec. III strongly suggests that the fixed point of the reduced averaged equations is stable. If this fixed point is in fact asymptotically stable in the linear approximation, then the error between the averaged and exact solutions will be bounded for all time for solutions in the fixed point’s basin of attraction [35]. This would imply that the exact solution must stay confined to a neighborhood of the averaging fixed point. While we do not provide a mathematically rigorous proof that the fixed point is asymptotically stable, our numerical results shown in Fig. 6 and Fig. 7 are consistent with this hypothesis and the resulting stability of the exact solution.

The plots in Fig. 6 are consistent with these conclu-

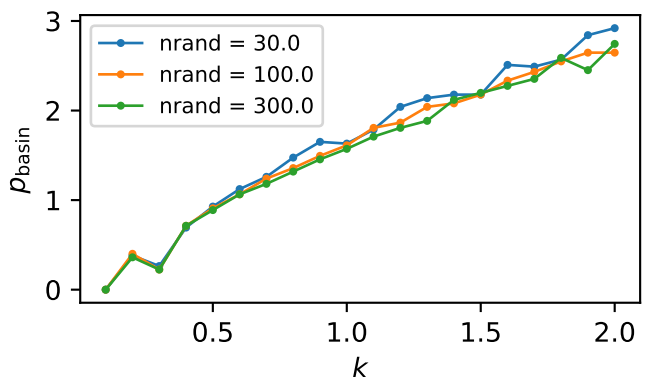


FIG. H14. Convergence study for the binary search algorithm used to determine the basin radius p_{basin} . The three curves show the results of the binary searches at each value of the coupling k for 30, 100, and 300 random initial conditions.

sions holding for a neighborhood of system parameter space around the baseline parameters. Changing the parameters across the ranges used in this study appears to result in systems that are topologically equivalent to the system at the baseline parameters (that is, the system is structurally stable), so that in this range the fixed point continues to exist.

APPENDIX H: Finding the radius of the basin of attraction

In this section we describe the methods used to find the phase space radius p_{basin} shown in Fig. 8.

1. Background: the trimer fixed point in 6D phase space

In order to understand what this means, we need to describe what the constant-amplitude state corresponding to the fixed point (32) represents in the full six-dimensional phase space of the unaveraged system (1). The averaging procedure described in section III captures this state as single point in a 2-dimensional phase space whose dimensions are the “slow” variables r and c (respectively, the amplitude of the oscillations and the phase offset). But in terms of the original variables x_j and $v_j = \dot{x}_j$, the steady state represented by the fixed point (32) is a closed curve in 6D phase space. Using Eq. (11) and the coordinate changes Equations (5) and (6), we can write the positions and velocities corresponding to the ansatz (9) at the fixed point:

$$x_j = r_* \cos \left(\omega t + c_* - \frac{2\pi(j-1)}{3} \right) \quad (\text{H1})$$

$$v_j = -\omega r_* \sin \left(\omega t + c_* - \frac{2\pi(j-1)}{3} \right) \quad (\text{H2})$$

The coordinates and velocities are periodic functions of time, so the state (32), which is a fixed point in r - c space, is a closed loop in x - v phase space.

We are interested in the set of points that converge to this loop-shaped attractor under the phase flow of the equations of motion Eq. (1). In particular, we would like some indication that this is an open set, and how large it is for different values of the parameters, especially the coupling k . While we will not check explicitly for convergence to this phase space loop, we will check for convergence of the trajectory *amplitudes* to the amplitude r_* given in Eq. (32), which is common to all three oscillators when they reach the loop. In this work, we take the convergence of trajectories to trajectories having this *amplitude* as a reasonable proxy for convergence to the loop attractor predicted by averaging.

2. Defining the radius of the basin of attraction

We define the *basin of attraction of the fixed point amplitude* as the set of all points $(x_1, x_2, x_3, v_1, v_2, v_3)$ that flow to oscillatory steady states having the amplitude r_* given in Eq. (32). We will abuse notation and refer to this set as the “basin of attraction,” although strictly speaking it is not the basin of attraction of the averaging loop attractor because it makes no reference to the oscillation phases. The basin of attraction is a subset of \mathbb{R}^6 , and could have a complicated shape. As a simple indicator of the size of the basin, we define the *radius of the basin*, p_{basin} , as the minimum distance from a particular point $\vec{y}_* \in \mathbb{R}^6$ on the loop attractor to the edge of the basin; we write \vec{y}_* as $y_* = (\vec{x}_*, \vec{v}_*)$ with $\vec{x}_*, \vec{v}_* \in \mathbb{R}^3$ given by

$$x_{*j} = r_* \cos(c_* + 2\pi(j-1)/3), \quad (\text{H3})$$

$$v_{*j} = -\omega r_* \sin(c_* + 2\pi(j-1)/3) \quad (\text{H4})$$

$(j = 1, 2, 3)$

These are the values of x_j and v_j from Eq. (H1) and Eq. (H2) evaluated at $t = 0$.

3. Finding the basin radius as a function of k

We begin by defining the *indicator function* $f_I(p)$ to be 0 if any point at distance p from y_* converges to a state with the fixed-point amplitude r_* , and 1 otherwise. In other words, the indicator function is 0 if the phase-space sphere of radius p is entirely within the basin of attraction, and 1 if any portion of it lies outside the basin. Note that the indicator function is a step function with the discontinuity at the basin radius, since it evaluates to 0 for any $p < p_{\text{basin}}$ and to 1 for $p > p_{\text{basin}}$.

We cannot compute the phase flow of every point in the sphere centered at y_* , so to implement f_I in practice we compute the trajectories of 300 randomly-chosen initial conditions that lie in 5D hypersurface. We chose the value 300 by conducting a convergence study with

30, 100, and 300 points, the results of which are shown in Fig. H14. We chose each point by using Numpy’s `standard_normal` function to generate a vector of six coordinates drawn from the standard normal distribution and then normalizing the vector to have the desired length. This procedure gives each point of the 5D sphere the same probability of being selected because the joint probability density for selecting each vector in this way depends only on the radius of the sphere: $e^{-(y_1-y_{*1})^2} \dots e^{-(y_6-y_{*6})^2} = e^{-|\vec{y}-\vec{y}_*|^2} = e^{-p^2}$.

For these integrations, we used numpy’s `solve_ivp` with the integration parameters described in Appendix B. We used the trimer parameters given in the caption of Fig. 8 with an integration time of 2000 dimensionless time units. We considered any state with an amplitude within 0.01 dimensionless distance units of r_* to have converged in amplitude to r_* , and all other trajectories to not have converged. As throughout this work, we compute the amplitudes of each oscillator as the maximum displacement attained by that oscillator over a time interval near the end of the integration window; for these trajectories, we used the last 40 dimensionless time units.

We use a binary search procedure to efficiently find p_{basin} using the indicator function. We first set a high upper limit L on the value of the basin radius by evaluating the indicator function over a coarse, equally-spaced range of values of p beginning at zero; for the searches described here, we chose $L = 5$. We also decide on the precision ϵ_p to which we wish to know p_{basin} ; in these searches we used $\epsilon_p = 0.01$. To complete the search we evaluate $f_I(p)$ n_{eval} times, on values $\{p_1 = L/2, p_2, \dots, p_{n_{\text{eval}}}\}$, where n_{eval} is the smallest integer such that $L/2^{(n_{\text{eval}}+1)} \leq \epsilon_p$. We then find the values of p_n iteratively as follows:

$$p_1 = L/2$$

$$p_{n+1} = \begin{cases} p_n + L/2^{n+1}, & f_I(p_n) = 0 \\ p_n - L/2^{n+1}, & f_I(p_n) = 1 \end{cases} \quad (\text{H5})$$

The found value of p_{basin} is $p_{n_{\text{eval}}+1}$ according to the rule above.

We used this procedure to find p_{basin} for $k = \{0.1, 0.2, \dots, 2\}$, producing the curve shown in the upper panel of Fig. 8. The lower two panels show the p -values chosen by the binary search algorithm for two selected values of k .

One might suggest the simpler procedure of evaluating f_I on a grid of equally-spaced points p_n between 0 and L . With this method, the number of required evaluations scales linearly as L/ϵ_p . This makes it considerably more expensive than the binary search method, where $n_{\text{eval}} \sim \log(L/\epsilon_p)$.

TABLE I. Material and structural parameters used for the plate resonator model in COMSOL.

Parameter	Value
Plate thickness	0.345 nm
Poisson ratio	0.456
Young's modulus	1×10^{12} Pa
Density	1.8 g/cm^3
Base in-plane stress, σ_0	1×10^7 Pa

APPENDIX I: Finite-element simulation of elastic resonator trimer

The full-wave simulations of the coupled membrane resonators was implemented using the scientific analysis software COMSOL Multiphysics, version 6.2. We recreated a trio of resonators by defining an equilateral triangular elastic plate with a side length of 16.5 microns and punching out an inverted triangular hole in its center of side length 3 microns. Normal line segments from the corners of the inner hole to the nearest outer edges defined three quadrilateral regions. The fundamental vibrational mode of each quadrilateral defines an oscillator degree of freedom, coupled to its neighbors by the continuous plate material. We chose structural and material parameters to recreate typical values for MEMS resonators based on low-dimensional materials such as graphene, listed in Table I.

Full three-dimensional thin-plate dynamics were implemented using a Shell interface in the Structural Mechanics module in COMSOL, which uses second-order Lagrange finite elements. The finite-element mesh was automatically generated in COMSOL using the ‘Physics-controlled’ option with ‘Extremely fine’ element size, producing a mesh with 2490 triangular elements. Clamped boundary conditions were imposed on the edges of the outer and inner triangles. Crucially, we used a linear elastic material for the thin-shell dynamics, but included geometric nonlinearity which couples the in-plane strains u_{ij} of the midsurface with transverse deformations $h(x, y)$ via the strain component

$$u_{ij} = \frac{1}{2} \partial_i h \partial_j h.$$

This geometric nonlinearity provides two mechanisms that are crucial for the discrete model dynamics to be recreated: it allows the fundamental mode frequency of each resonator to be modulated dynamically by varying the in-plane tension; and it generates a stiffening nonlinearity in the dynamics of the transverse field. These mechanisms are generic to plate resonators regardless of material, and in particular they do not rely on nonlinear elasticity at the material level.

To identify the relevant mode frequency for parametric modulation, we first carried out a pre-stressed eigenfrequency study by applying a uniform in-plane isotropic stress $\sigma_{xx} = \sigma_{yy} = \sigma_0 = 1 \times 10^7$ Pa and computing

the lowest six eigenmodes of the plate. The lowest three eigenmodes are well-separated from the higher modes, with the frequencies of modes two and three nearly identical (Fig. 9(b)); this mirrors the expectation from coupling the fundamental modes on each resonator as in Fig. 1. However, COMSOL does not decompose the degenerate subspace into the clockwise and counterclockwise-rotating modes, but rather into arbitrary linear combinations of them with the degeneracy lifted by the mesh.

To recreate the dynamics of the discrete model in the elastic system, we modulated the in-plane prestresses within each of the three quadrilateral domains (indexed by j) as

$$\sigma_j(t) = \sigma_0 \left[1 + \delta' \cos \left(2\omega_1 t + \frac{2\pi}{3} j \right) \right].$$

The system is initialized with displacements from the second eigenmode (which overlaps with, but is not exactly parallel to, the parametrically amplified mode). The *generalized alpha* solver, standard for inertial dynamics in COMSOL, was used in a time-dependent study with a relative tolerance of 10^{-5} . We measured the vertical displacements at the centroids of the three quadrilaterals as a proxy for the amplitude of the out-of-plane deflections of the three resonators. For the runs shown in Fig. 9, we generated trajectories 30 microseconds long in COMSOL, recording the oscillator displacements at time steps spaced by 0.01 microseconds. The spacing of the internal time steps is much smaller and set adaptively by COMSOL to meet the specified tolerance.

APPENDIX J: Fitting procedure for Figure 9

Below we describe the procedure used to produce the trajectory of the reduced averaged equations (the red curve) in Figure 9. We obtain this curve by integrating Eq. (10). We restore the nonlinearity parameter α to the trimer equations of motion for this section as described in Appendix A, Eq. (A7).

The procedure in this section finds values for values of δ , ω , ϵ , and α to be used in Eq. (10). We assume resonance conditions, as are used to generate the FEM traces: $\gamma = 2\omega$.

1. Extract a single amplitude trace from the three continuum traces

The finite element method (FEM) traces are produced by recording the vertical displacement of a particular point on each plate. We first process these three traces to produce a single amplitude trace. The procedure is as follows:

1. Numerically compute the local maxima of each continuum trace to obtain three amplitude traces.

2. Aggregate the three numerical amplitude traces to create a single trace, ordered by time.
3. Generate a piecewise-linear interpolant of the aggregated traces to establish a constant time increment.
4. Filter the interpolant with a Savitsky-Golay filter. We use the `savgol_filter` function of signal module within the Python library Scipy. This produces the FEM amplitude trace. We use a second-order filter with a window width corresponding to ten times the period $2\pi/\omega_0$ of the trimer fundamental mode. For Fig. 9, $\omega_0 = 52.607$ MHz.

2. Rescale time and length units in the continuum amplitude trace

Next, we rescale the time and amplitude coordinates of the FEM amplitude traces to make them dimensionless. The frequency scale for the FEM trace is the frequency ω_0 of the fundamental mode, which can be obtained directly as an output from Comsol. We rescale the time points from the FEM trace to be dimensionless by multiplying each time point by ω_0 . We choose to rescale the length units to be in units of the fixed point length R_* ; this is achieved by numerically computing the value of the fixed point amplitude and dividing all lengths by this value. We compute the value of the fixed point by finding the average value of the FEM amplitude trace over a time interval where it has converged; i.e., the oscillations about the fixed point have an amplitude that is a small fraction of the fixed point amplitude. For Fig. 9, we use the interval from $t = 27\mu s$ until the end of the trace as the converged interval. The computed fixed point amplitude is $R_* = 2.56824$ nm.

3. Fit a damped oscillation to the ringdown region

We first process the FEM amplitude trace in the ringdown region—the region where the trace amplitude undergoes damped oscillations about the fixed point—by subtracting out the fixed point value, so that the amplitude oscillates about 0. We then fit a decaying oscillation of the form

$$r(t) = Ae^{-\lambda t} \cos(\Omega_d t) \quad (\text{J1})$$

to the data in this region. For Fig. 9, we use the interval $15\mu s \leq t \leq 25\mu s$ as the ringdown region. The fit parameters are λ (the damping constant) and Ω_d (the damped frequency). We numerically extract the amplitude A by computing the maximum value of the amplitude of the filtered trace.

Now we use the fixed point formula Eq. (32) to establish relationships between the fit parameters and the

parameters of the trimer. We restore the nonlinearity parameter α to Eq. (32) to obtain

$$r_* = \sqrt{\frac{2}{3\alpha}} \left[\delta^2 - (2\omega\epsilon)^2 \right]^{1/4} \quad (\text{J2})$$

We then have that the fixed point r_* is

$$r_* = \sqrt{\frac{4\omega\Omega_{rd}}{3\alpha}} \quad (\text{J3})$$

where Ω_{rd} is the ringdown frequency from Eq. (27), ω is the ratio of the traveling wave frequency to the fundamental frequency, and α is the nonlinearity parameter. For the FEM system we use in Fig. 9, $\omega = 1.04297$. Recall that after rescaling as described in Subsection J2, $r_* = 1$, so α is dimensionless as it appears in this section.

Eq. (J1) is a solution to a damped harmonic oscillator equation of the form

$$\ddot{b} + 2\lambda\dot{b} + \Omega_{rd}^2 b = 0 \quad (\text{J4})$$

with

$$\Omega_d^2 = \Omega_{rd}^2 - \lambda^2 \quad (\text{J5})$$

Comparing to Eq. (26) and Eq. (27), we see that

$$\lambda = \epsilon/2 \quad (\text{J6})$$

4. Solve the above equations for all parameters except δ

First solve the Ω_d equation for Ω_{rd} :

$$\Omega_{rd} = \sqrt{\Omega_d^2 + \lambda^2} \quad (\text{J7})$$

Then use the result to isolate α :

$$\alpha = \frac{4\omega\Omega_{rd}}{3r_*^2} \quad (\text{J8})$$

We get ϵ directly from the parameter λ :

$$\epsilon = 2\lambda \quad (\text{J9})$$

5. Fit an exponential to the growth region and find δ

Fit a function of the form

$$r = r_0 e^{\kappa t} \quad (\text{J10})$$

to the growth region of the motion—the region where the amplitude is exponentially growing. We use $5\mu s \leq t \leq 8\mu s$ as the growth region for Fig. 9.

After fitting an exponential to the FEM amplitude in this region, we have

$$\kappa = \frac{1}{2} \left(\frac{\delta}{2\omega} - \epsilon \right) \quad (\text{J11})$$

which gives

$$\delta = 2\omega(2\kappa + \epsilon) \quad (\text{J12})$$

Since ϵ is known from the previous fit, the parameters of the discrete trimer model are now fully determined. For the fit in Fig. 9, the resulting parameters are

$$\begin{aligned} \alpha &= 0.05874 \\ \delta &= 0.09677 \\ \epsilon &= 0.01318 \end{aligned} \quad (\text{J13})$$

6. Find the correct initial conditions and integrate

To obtain the amplitude curve, we numerically integrate Eq. (10). But first, we need to translate the FEM system initial conditions into initial conditions for the reduced averaged equations. Note that since the ansatz used to obtain the reduced averaged equations from the averaged equations is

$$A_j = A e^{-2\pi i(j-1)/3}, \quad (\text{J14})$$

the reduced averaged amplitude A corresponds to the amplitude A_1 of the full averaged equations. A_1 is distinguished from the other amplitudes by having no phase

offset in its parametric modulation term. This means we can use the position $x_{\text{FEM},1}$ and velocity $\dot{x}_{\text{FEM},1}$ of the corresponding FEM oscillator (i.e., the one with no phase offset in its modulation term; see Eq. (36)) to determine initial conditions for A , via the coordinate transformation

$$A(0) = A_1(0) = \frac{1}{2}(x_{\text{FEM},1}(0) - i\dot{x}_{\text{FEM},1}(0)/\omega) \quad (\text{J15})$$

which we obtain from Eq. (5) and Eq. (6).

Once we have the correct initial conditions, we integrate Eq. (10), obtaining the complex amplitude $A(t)$. Recalling Eq. (11), the real amplitude is

$$r(t) = 2A(t). \quad (\text{J16})$$

7. Restore length and time units

As a final step before plotting, we restore the length and time units by multiplying each dimensionless length by R_* from Subsection J2 and each dimensionless time by $1/\omega_0$.

-
- [1] W. W. Mumford, Some notes on the history of parametric transducers, *Proceedings of the IRE* **48**, 848 (2007).
 - [2] A. Smith, R. Sandell, J. Burch, and A. Silver, Low noise microwave parametric amplifier, *IEEE Transactions on Magnetics* **21**, 1022 (1985).
 - [3] J. Aumentado, Superconducting parametric amplifiers: The state of the art in josephson parametric amplifiers, *IEEE Microwave magazine* **21**, 45 (2020).
 - [4] L.-A. Wu, M. Xiao, and H. Kimble, Squeezed states of light from an optical parametric oscillator, *Journal of the Optical Society of America B* **4**, 1465 (1987).
 - [5] D. Rugar and P. Grütter, Mechanical parametric amplification and thermomechanical noise squeezing, *Physical Review Letters* **67**, 699 (1991), publisher: American Physical Society.
 - [6] W. Louisell, *Coupled Mode and Parametric Electronics* (John Wiley & Sons, New York, 1960).
 - [7] A. Eichler and O. Zilberberg, *Classical and Quantum Parametric Phenomena* (Oxford University Press, 2023).
 - [8] A. Leuch, L. Papariello, O. Zilberberg, C. L. Degen, R. Chitra, and A. Eichler, Parametric symmetry breaking in a nonlinear resonator, *Physical review letters* **117**, 214101 (2016).
 - [9] J. F. Rhoads and S. W. Shaw, The impact of nonlinearity on degenerate parametric amplifiers, *Applied Physics Letters* **96** (2010).
 - [10] L. Papariello, O. Zilberberg, A. Eichler, and R. Chitra, Ultrasensitive hysteretic force sensing with parametric nonlinear oscillators, *Physical Review E* **94**, 022201 (2016).
 - [11] Z. Wang, A. Marandi, K. Wen, R. L. Byer, and Y. Yamamoto, Coherent ising machine based on degenerate optical parametric oscillators, *Physical Review A* **88**, 063853 (2013).
 - [12] A. Marandi, Z. Wang, K. Takata, R. L. Byer, and Y. Yamamoto, Network of time-multiplexed optical parametric oscillators as a coherent Ising machine, *Nature Photonics* **8**, 937 (2014).
 - [13] P. L. McMahan, A. Marandi, Y. Haribara, R. Hamerly, C. Langrock, S. Tamate, T. Inagaki, H. Takesue, S. Utsunomiya, K. Aihara, R. L. Byer, M. M. Fejer, H. Mabuchi, and Y. Yamamoto, A fully programmable 100-spin coherent Ising machine with all-to-all connections, *Science* **354**, 614 (2016).
 - [14] T. L. Heugel, O. Zilberberg, C. Marty, R. Chitra, and A. Eichler, Ising machines with strong bilinear coupling, *Physical Review Research* **4**, 013149 (2022).
 - [15] M. Calvanese Strinati, L. Bello, A. Pe'er, and E. G. Dalla Torre, Theory of coupled parametric oscillators beyond coupled ising spins, *Physical Review A* **100**, 023835 (2019).
 - [16] M. Calvanese Strinati, L. Bello, E. G. Dalla Torre, and A. Pe'er, Can nonlinear parametric oscillators solve random ising models?, *Physical Review Letters* **126**, 143901 (2021).
 - [17] T. L. Heugel, M. Oscity, A. Eichler, O. Zilberberg, and R. Chitra, Classical Many-Body Time Crystals, *Physical Review Letters* **123**, 124301 (2019), publisher: American Physical Society.

- [18] N. Y. Yao, C. Nayak, L. Balents, and M. P. Zaletel, Classical discrete time crystals, *Nature Physics* **16**, 438 (2020).
- [19] S. Yi-Thomas and J. D. Sau, Theory for dissipative time crystals in coupled parametric oscillators, *Physical Review Letters* **133**, 266601 (2024).
- [20] R. Lifshitz and M. Cross, Response of parametrically driven nonlinear coupled oscillators with application to micromechanical and nanomechanical resonator arrays, *Physical review B* **67**, 134302 (2003).
- [21] R. Lifshitz and M. C. Cross, Nonlinear dynamics of nanomechanical and micromechanical resonators, *Reviews of nonlinear dynamics and complexity* **1**, 1 (2008).
- [22] G. Margiani, O. Ameye, O. Zilberberg, and A. Eichler, Three strongly coupled kerr parametric oscillators forming a boltzmann machine, *Physical Review Letters* **135**, 097201 (2025).
- [23] O. Ameye, A. Eichler, and O. Zilberberg, The parametric instability landscape of coupled Kerr parametric oscillators (2025), arXiv:2501.08793 [cond-mat].
- [24] L. Bello, M. Calvanese Strinati, E. G. Dalla Torre, and A. Pe'er, Persistent Coherent Beating in Coupled Parametric Oscillators, *Physical Review Letters* **123**, 083901 (2019).
- [25] C. A. Downing, D. Zueco, and L. Martín-Moreno, Chiral Current Circulation and PT Symmetry in a Trimer of Oscillators, *ACS Photonics* 10.1021/acsphotonics.0c01208 (2020).
- [26] A. Melkani and J. Paulose, Space-time symmetry and nonreciprocal parametric resonance in mechanical systems, *Physical Review E* **110**, 015003 (2024).
- [27] N. Kruss and J. Paulose, Nondispersive One-Way Signal Amplification in Sonic Metamaterials, *Physical Review Applied* **17**, 024020 (2022).
- [28] A. Melkani and J. Paulose, Space-time Floquet operator: Non-reciprocity and fractional topology of space-time crystals (2025), arXiv:2510.16562 [cond-mat].
- [29] F. Zangeneh-Nejad and R. Fleury, Active times for acoustic metamaterials, *Reviews in Physics* **4**, 100031 (2019).
- [30] E. Ventsel and T. Krauthammer, *Thin Plates and Shells: Theory, Analysis, and Applications* (Taylor & Francis Group, 2001).
- [31] P. Karki and J. Paulose, Stopping and Reversing Sound via Dynamic Dispersion Tuning in a Phononic Metamaterial, *Physical Review Applied* **15**, 034083 (2021), publisher: American Physical Society.
- [32] V. Yakubovich, V. Starzhinskii, and G. Schmidt, *On Linear Differential Equations with Periodic Coefficients*, Vol. 1 (Wiley, London, 1976) pp. 222–222.
- [33] L. D. Landau and E. M. Lifshitz, *Mechanics*, 2nd ed., Vol. 1 (Butterworth Heinemann, 1960).
- [34] S. H. Strogatz, *Nonlinear dynamics and Chaos: with applications to physics, biology, chemistry, and engineering*, Studies in nonlinearity (Addison-Wesley Pub, Reading, Mass, 1994).
- [35] J. A. Sanders, F. Verhulst, J. A. Murdock, and J. Murdock, *Averaging methods in nonlinear dynamical systems*, 2nd ed., Applied mathematical sciences No. 59 (Springer, New York, NY, 2007).
- [36] J. Guckenheimer, Dynamics of the Van der Pol equation, *IEEE Transactions on Circuits and Systems* **27**, 983 (1980).
- [37] I. Kovacic, R. Rand, and S. Mohamed Sah, Mathieu's equation and its generalizations: overview of stability charts and their features, *Applied Mechanics Reviews* **70**, 020802 (2018).
- [38] We add an overall $(-)$ sign to the phases because the amplified mode travels in the direction opposite the modulation wave [26].
- [39] When $\Delta\gamma \neq 0$, this quantity is no longer conserved and there are no longer closed orbits, but in the extended phase space each time slice of the flow field is identical—up to a shift in the phase offset c —to the resonance flow field by Eq. (12).
- [40] M. Abramowitz and I. A. Stegun, *Handbook of mathematical functions with formulas, graphs, and mathematical tables*, Vol. 55 (US Government printing office, 1948).
- [41] I. Mahboob and H. Yamaguchi, Bit storage and bit flip operations in an electromechanical oscillator, *Nature Nanotechnology* **3**, 275 (2008).
- [42] I. Mahboob, M. Mounaix, K. Nishiguchi, A. Fujiwara, and H. Yamaguchi, A multimode electromechanical parametric resonator array, *Scientific Reports* **4**, 4448 (2014).
- [43] J. P. Mathew, R. N. Patel, A. Borah, R. Vijay, and M. M. Deshmukh, Dynamical strong coupling and parametric amplification of mechanical modes of graphene drums, *Nature Nanotechnology* **11**, 747 (2016).
- [44] M. J. Seitner, M. Abdi, A. Ridolfo, M. J. Hartmann, and E. M. Weig, Parametric Oscillation, Frequency Mixing, and Injection Locking of Strongly Coupled Nanomechanical Resonator Modes, *Physical Review Letters* **118**, 254301 (2017).
- [45] J. M. Miller, D. D. Shin, H.-K. Kwon, S. W. Shaw, and T. W. Kenny, Phase Control of Self-Excited Parametric Resonators, *Physical Review Applied* **12**, 044053 (2019).
- [46] L. Mestre, S. Singh, G. Margiani, L. Catalini, A. Eichler, and V. Dumont, A network of parametrically driven silicon nitride mechanical membranes (2025), arXiv:2506.00850 [cond-mat].
- [47] P. Prasad, N. Arora, and A. K. Naik, Parametric amplification in MoS₂ drum resonator, *Nanoscale* **9**, 18299 (2017).
- [48] S. Naserbakht, A. Naesby, and A. Dantan, Stress-Controlled Frequency Tuning and Parametric Amplification of the Vibrations of Coupled Nanomembranes, *Applied Sciences* **9**, 4845 (2019).
- [49] Z.-J. Su, Y. Ying, X.-X. Song, Z.-Z. Zhang, Q.-H. Zhang, G. Cao, H.-O. Li, G.-C. Guo, and G.-P. Guo, Tunable parametric amplification of a graphene nanomechanical resonator in the nonlinear regime, *Nanotechnology* **32**, 155203 (2021).
- [50] A. M. v. d. Zande, R. A. Barton, J. S. Alden, C. S. Ruiz-Vargas, W. S. Whitney, P. H. Q. Pham, J. Park, J. M. Parpia, H. G. Craighead, and P. L. McEuen, Large-scale arrays of single-layer graphene resonators, *Nano Letters* **10**, 4869 (2010).
- [51] J. Cha, K. W. Kim, and C. Daraio, Experimental realization of on-chip topological nanoelectromechanical metamaterials, *Nature* **564**, 229 (2018).
- [52] B. Carter, U. F. Hernandez, D. J. Miller, A. Blaikie, V. R. Horowitz, and B. J. Alemán, Coupled Nanomechanical Graphene Resonators: A Promising Platform for Scalable NEMS Networks, *Micromachines* **14**, 2103 (2023).
- [53] J. Cha and C. Daraio, Electrical tuning of elastic wave propagation in nanomechanical lattices at mhz frequencies, *Nature Nanotechnology* **13**, 1016 (2018).
- [54] T. Mei, J. Lee, Y. Xu, and P. X.-L. Feng, Frequency tuning of graphene nanoelectromechanical resonators via

- electrostatic gating, *Micromachines* **9**, 312 (2018).
- [55] A. Blaikie, D. Miller, and B. J. Alemán, A fast and sensitive room-temperature graphene nanomechanical bolometer, *Nature Communications* **10**, 1 (2019).
- [56] B. Apffel and R. Fleury, Experimental observation of topological transition in linear and nonlinear parametric oscillators, *Physical Review E* **109**, 054204 (2024).
- [57] T. Inagaki, Y. Haribara, K. Igarashi, T. Sonobe, S. Tamate, T. Honjo, A. Marandi, P. L. McMahon, T. Umeki, K. Enbutsu, O. Tadanaga, H. Takenouchi, K. Aihara, K.-i. Kawarabayashi, K. Inoue, S. Utsunomiya, and H. Takesue, A coherent Ising machine for 2000-node optimization problems, *Science* **354**, 603 (2016).
- [58] R. Fleury, D. L. Sounas, C. F. Sieck, M. R. Haberman, and A. Alù, Sound Isolation and Giant Linear Nonreciprocity in a Compact Acoustic Circulator, *Science* **343**, 516 (2014).
- [59] H. Nassar, B. Yousefzadeh, R. Fleury, M. Ruzzene, A. Alù, C. Daraio, A. N. Norris, G. Huang, and M. R. Haberman, Nonreciprocity in acoustic and elastic materials, *Nature Reviews Materials* , 1 (2020).
- [60] P. Virtanen, R. Gommers, T. E. Oliphant, M. Haberland, T. Reddy, D. Cournapeau, E. Burovski, P. Peterson, W. Weckesser, J. Bright, S. J. van der Walt, M. Brett, J. Wilson, K. J. Millman, N. Mayorov, A. R. J. Nelson, E. Jones, R. Kern, E. Larson, C. J. Carey, Í. Polat, Y. Feng, E. W. Moore, J. VanderPlas, D. Laxalde, J. Perktold, R. Cimrman, I. Henriksen, E. A. Quintero, C. R. Harris, A. M. Archibald, A. H. Ribeiro, F. Pedregosa, P. van Mulbregt, and SciPy 1.0 Contributors, SciPy 1.0: Fundamental Algorithms for Scientific Computing in Python, *Nature Methods* **17**, 261 (2020).